

Department of Construction Sciences
Solid Mechanics

ISRN LUTFD2/TFHF-20/5236-SE(1-67)

Orientation dependant grain boundary diffusion in polycrystals

Master's Dissertation by

Kevin Hult Blixt

Supervisor:
Håkan Hallberg, Division of Solid Mechanics

Examiner:
Mathias Wallin, Division of Solid Mechanics

Copyright © 2020 by the Division of Solid Mechanics
and Kevin Hult Blixt

For information, address:
Division of Solid Mechanics, Lund University, Box 118, SE-221 00 Lund, Sweden
Webpage: www.solid.lth.se

Abstract

Grain boundary diffusion in polycrystals is of importance in industrial applications as it often, to a large degree, dictates the effective rate of diffusion in polycrystals. For impurity diffusion the enrichment of impurities within the material will in turn change the material properties, such as ductility and fatigue rates. It is therefore beneficial to be able to quantify the effect of the grain boundaries on diffusion rates. This relates to the field of grain boundary engineering, whereby control of material parameters, such as the crystallographic texture, desired grain boundary properties and in extension material properties, are achieved.

In this thesis a texture sensitive model for the rate of diffusion is derived and employed in finite element simulations of polycrystals. The developed model was found to correlate well with available data. Utilising the model, constant source diffusion is studied for different textures. The results show that the effective diffusion varies depending on the texture, consistent with previous studies.

Furthermore, a classical slab model was compared to an exponential model for the distribution of the grain boundary diffusivity and a large difference in the resulting penetration profiles were found. The common experimental methods used to extract diffusion coefficients was examined using simulations and were found to give poor results for type B and C diffusion kinetics, whereas the results for type A diffusion were satisfactory.

Difficulties were found regarding the lack of available experimental data, or the lack of some specific details in available data. The most prominent problem was the lack of accompanying texture data to that of polycrystal diffusion experiments. As such, a matching simulation to that of an experiment could not be made.

“There is a crack in everything. That’s how the light gets in.” - Leonard Cohen

Preface

The subject of this work was suggested by the supervisor Håkan Hallberg in a conversation with the author and was made possible by the Division of Solid Mechanics at LTH by providing a workspace, computer and free coffee. At least at the start as the world was later struck by the outbreak of the covid-19 pandemic and it was decided that everybody should work from home. This has not been seen as a major setback due to the computer based methodology of this work and availability of online resources.

The subject was partly chosen out of the supervisors curiosity as he had not been working directly with the subject of diffusion, but instead on other related subjects and partly of the fact that it did not seem to be a large pool of papers regarding finite element simulations of the kind done in this work, or other mesoscale calculations of diffusion behaviour in polycrystals.

Acknowledgement

This work would not have come to fruition if not for my supervisor Håkan Hallberg. I would like to express my gratitude towards his kindness and willingness to help throughout this project, even though these words are not enough to convey that.

Contents

1	Introduction	1
1.1	Why bother?	1
1.2	Objectives	2
1.3	Limitations and restrictions	2
1.4	Method	2
1.5	Report structure	3
2	Polycrystalline materials and diffusion mechanisms	4
2.1	Crystal systems	4
2.1.1	Description of the crystallographic orientation	5
2.2	Grain boundaries	6
2.2.1	Texture and grain boundary specification	7
2.2.2	Tilt and twist, the decomposition of rotation	8
2.3	Transient diffusion described by Fick's second law	8
2.3.1	Analytical solutions to Fick's second law	9
2.4	Lattice diffusion	9
2.4.1	Interstitial diffusion mechanism	10
2.4.2	Vacancy diffusion mechanism	10
2.4.3	Other diffusion mechanisms	11
2.4.4	Externally applied forces	11
2.4.5	Temperature dependence of diffusion described by the Arrhenius relation	12
2.5	Grain boundary diffusion	12
2.5.1	Misorientation and disorientation	12
2.5.2	Grain boundary interfaces	13
2.5.3	Segregation	14
2.6	The Fisher model, an analytical approach to grain boundary diffusion	14
2.6.1	Whipple's solution	15
2.6.2	The extended Fisher model and Harrison A, B and C diffusion kinetics regimes	15
2.7	Experimental methods for measuring the diffusion coefficient	17
2.7.1	Radiotracer diffusion and the serial sectioning method	17
3	Grain orientation dependent diffusion	20
3.1	Grain boundary energy	20
3.1.1	The dislocation model	20
3.1.2	The Read–Shockley relation	21
3.1.3	Coincident site lattice (CSL)	23
3.1.4	The Brandon criteria	25
3.1.5	Read–Shockley relation with CSL consideration	25
3.1.6	An interpolation approach, taking all five macroscopic degrees of freedom into consideration	26

3.2	Relationship between grain boundary energy and excess volume	27
3.3	From grain boundary energy to the diffusion coefficient	29
4	Computational and numerical framework	33
4.1	Finite element formulation	33
4.1.1	Determining the diffusion coefficient of the element using barycentric coordinates . . .	33
4.1.2	Solving the first order differential equation	35
4.2	Level set formulation	35
4.3	Grain boundary diffusion coefficient distribution	36
5	Simulation of diffusion in a bicrystal	38
5.1	Model geometry and meshing	38
5.2	Convergence study using the exponential model	40
5.3	Comparison between Whipple's solution and a FE-solution	41
5.4	Extraction of grain boundary diffusion coefficients from penetration profiles	42
5.4.1	Type A diffusion	42
5.4.2	Type B diffusion	43
5.4.3	Type C diffusion	44
5.4.4	Discussion	45
6	Simulation of diffusion in a polycrystal	46
6.1	Model geometry and meshing	46
6.2	Convergence study	47
6.3	Comparison with experiments	48
6.4	Extraction of grain boundary diffusion coefficients from penetration profiles	52
6.4.1	Type A diffusion	52
6.4.2	Type B diffusion	53
6.4.3	Type C diffusion	54
6.4.4	Discussion	54
7	Summary, conclusions and closing remarks	55
7.1	Grain orientation dependent diffusion	55
7.2	Measurements of the diffusion coefficient	55
7.3	What the future holds	55
	Bibliography	57

Chapter 1

Introduction

This report studies diffusion in metals that contains grain boundaries, where the dissimilar structure between neighboring grains create misfit dislocations at the grain boundaries that act as highways for diffusing atoms. Because of this increased diffusivity, the grain boundaries, though relatively narrow, have a noticeable effect on the system mechanics, such as the effective rate of impurity diffusion. However, the rate of diffusion at the grain boundary has been found to be, amongst other things, orientation dependent [7, 3, 19, 37, 29] and it is therefore desirable to be able to determine grain boundary properties from material properties combined with the crystal orientations, i.e. the crystallographic texture, instead of using a constant value for all boundaries. However, this has proved to be difficult and has not been solved to date though promising leads have been found and tested in this work. Furthermore, the developed computer model is used to test assumptions that are frequently used in experimental studies when determining diffusion coefficients for constant sources.

In this chapter the objectives, limitations and restrictions, the employed methods as well as the report structure is presented. However, as a point of departure, these sections are preceded by a general discussion on the field of diffusion in polycrystal materials.

1.1 Why bother?

This section contains a few short examples of where the understanding of diffusion, and by extension grain boundary diffusion, is beneficial and motivates the study of this phenomena. These are related both to that of impurity diffusion and self-diffusion. For which self-diffusion considered one-component diffusion processes, where the diffusing atoms are the same as the bulk material. Impurity diffusion, on the other hand, considers processes for which the diffusing matter is different from the bulk material.

There are other phenomena, such as Coble creep and sintering, that are also dependent on grain boundary diffusion [23]. However, these are not discussed further in this report. Furthermore, the theories, methods and problems mentioned in this report are also related to other phenomena related to grain boundaries, such as grain boundary migration [17]. The grain boundary energy, which will be related to the grain boundary diffusion in terms of the boundary excess volume, is also related to the diffusion-coupled processes.

Let's start by considering one of the most recognized impurity diffusion phenomena, hydrogen diffusion, which cause embrittlement, and might be considered the poster child for diffusion in metals as it is "widely encountered" in every day life. The small size of hydrogen atoms makes it relatively easy for hydrogen to penetrate into other materials, not just metals. This is of importance in, for example, welding, where hydrogen is one of the factors that result in cold cracking [28]. It also results in faster fatigue crack growth rates when the weld is surrounded by hydrogen, be that hydrogen gas in pipelines [52] or water in nuclear reactors [56] or offshore structures [41]. Structures we most definitely do not want to crack unexpectedly during operation, making the understanding of these processes important.

The subject of diffusion also has relevance in the field of electronics and the phenomena of electromigration. This is a process whereby an electric current induces self-diffusion which might result in premature

failure of electric components [34], electromigration becomes even more important to be considered as the size of electric components are constantly reduced.

Furthermore, the space industry is in need of refractory materials, which are materials that have good material properties even at very high temperatures, for use in, amongst other things, nuclear power sources and population systems. These materials include, for example, tungsten and molybdenum. There are applications in which these metals are layered in order to utilise each material's strength. As these materials operate at high temperatures and under extended periods of time, diffusion between layers is inevitable. The expected life of these components is correlated to the diffusion between layers and has been reported to be the primary cause of failure [19].

Finally, diffusion affects the grain boundary structure and in turn grain growth and macroscopic properties such as, for example, the plastic behavior. Generally, most of what has been mentioned ties into the field of grain boundary engineering, whereby attractive material properties can be obtained from the knowledge and application of, for example, diffusion. However, improvements can also be unintentional. For example, it has been shown that the diffusion of copper in solar cells plays an important role in its efficiency and is an unexpected, and unintended, positive effect of using a copper back-plate [1].

1.2 Objectives

The objective of this thesis is to develop and test a texture sensitive diffusion model and to implement it as a numerical model in a finite element setting. The aim for the developed finite element model was to study multiple grain boundary phenomena, such as diffusion under grain growth. This was the main reason for using a level-set description of the grain structure. However, due to time limitations, this capability is not utilised in the present work although advantage is still taken of some aspects of the level set formulation.

1.3 Limitations and restrictions

Diffusion processes are complex and must for this reason be simplified by considering some restrictions on its formulation. Limitations also naturally exist in the chosen methods and theories used. Some examples, in no particular order, are:

- Not taking segregation into consideration during simulations
- Using stationary boundaries and not looking at the influence of moving boundaries
- Assuming that Fick's law of diffusion is valid, which may not always be the case [51]
- Only considering cubic crystal systems, primarily face center cubic systems

Furthermore, there are multiple surface conditions that can be applied for diffusion. The two most common found in the literature is either constant source or instantaneous source, also known as the thin layer condition. Only constant sources are considered in this work. Other conditions have been devised to more accurately describe a realistic scenario, for example the fast surface diffusion condition proposed by Mishin and Razumovskii [39].

Other limitations and restriction, other than those mentioned here, are noted throughout the paper.

1.4 Method

In this paper a geometry and material-sensitive expression for the grain boundary diffusion coefficient is developed and tested on different two dimensional (2D) structures. Both a bicrystal and a larger polycrystal are considered. 2D structures are used both for convenience and as almost all prominent features of grain boundary diffusion are available without a need for studies of three dimensional (3D) structures, with the exception for triple line junctions, as will be discussed later. The bicrystal, which is the simplest polycrystal

possible, is used to study the diffusion mechanics in crystals, both experimentally and theoretically, where a simple geometry is preferential. Much of the theories used, for example, for the calculation of diffusion coefficients from experiments, are derived analytically from a bicrystal model. Therefore, these analytical models will be compared with the model developed by the author. This report is not the first to do simulations of the diffusion behaviour in polycrystals, other studies comprise for example [31, 62], though this is one of the few doing it while also considering the fully anisotropic grain boundary character, a similar study is found in the work by Moghadam et al. [40].

1.5 Report structure

In the following chapter, chapter 2, the phenomenological aspects of diffusion, as well as grain boundary structure and measurement techniques are discussed. The third chapter discusses orientation dependent grain boundary energy, excess volume and presents the proposed structure- and material-dependent model for the diffusion coefficient. The proposed model is also compared to experimental data taken from the literature. This is followed, in chapter 4, by details on the specific computational models and methodologies used in this work. Next, simulations of bicrystals, in chapter five, and polycrystals, in chapter six, are investigated using the proposed model. The methodologies commonly found in experimental methods for constant sources are also investigated. A short summary is provided in the final chapter together with conclusions and closing remarks.

Chapter 2

Polycrystalline materials and diffusion mechanisms

Polycrystalline materials are, as the name suggests, materials that are made up of multiple crystallites, often referred to as “grains”, formed, for example, during the solidification of metals. Each grain itself has a regular ordered atomic structure, the crystal lattice, aside from possible local variation from precipitates, voids and dislocations. However, the grain may be distinguished from surrounding grains in terms of the crystal orientations. A grain boundary can thereby be defined as the narrow region over which the orientation of one grain changes into that of the adjacent grain. Polycrystalline materials include many of the materials in use today such as all common metals and alloys, some ceramics, rocks and ice. However, this study is only concerned with metals, primarily those with a face-centered cubic (FCC) structure.

This chapter serves as an introduction to the structure and geometrical descriptions of polycrystal materials, as well as diffusion mechanism, its mathematical description and experimental methods used to measure the diffusion properties of polycrystals.

2.1 Crystal systems

Crystal systems, i.e. the atomic lattice structure of a particular material, can take many forms but only cubic systems, such as the simple cubic (SC), the body-centered cubic (BCC) and especially face-centered cubic (FCC), all shown in figure 2.1, are considered in this work. In addition to the cubic structures, hexagonal, skew and other non symmetrical lattice structures exist. These structures all have a definable unit-cell, which is the building block of the crystal lattice, of which three examples are seen in figure 2.1. FCCs include materials such as copper, silver and nickel and BCCs includes for example vanadium and chromium. However, some substances, such as iron, can be ordered in a number of alternative crystal structures, depending on, for example, the thermal processing history [36].

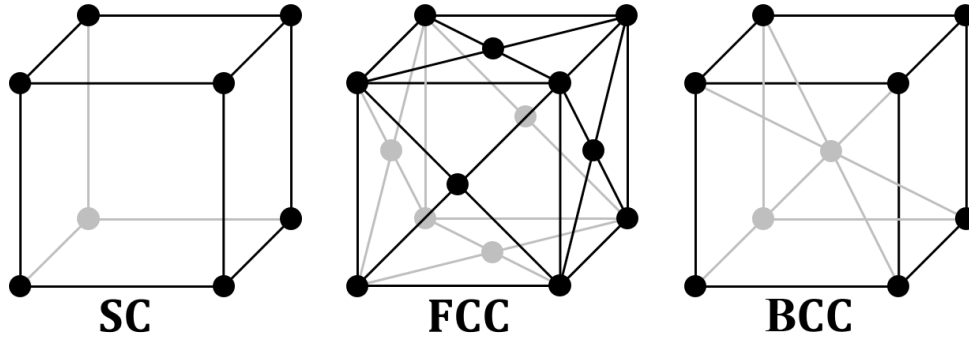


Figure 2.1: Simple cubic (SC), face-centered cubic (FCC) and body-centered cubic (BCC) unit cells, where each circle represent an atom, or lattice point. Repeated stacking of the unit cells in 3D provides the structure of the crystal systems.

2.1.1 Description of the crystallographic orientation

A systematic treatment of crystal coordinates and orientations becomes necessary when considering properties that vary with the lattice structure. There are multiple ways to describe the orientation of crystals. However, the use of Miller indices and Euler angles is often sufficient.

Miller index

The Miller index notation can be used to define planes as well as directions in crystal structures. Three coordinates are needed, usually denoted by hkl , and describe a multiple of the base vectors of the lattice unit cell. This is analogous to ordinary use of vectors to describe both directions and planes, with the sole exception being the specific choice of base vectors.

In figure 2.2 three planes within a cubic unit cell is shown, together with the corresponding base vectors and the Miller indices that describes the planes. What the Miller index entails are noted by the type of parentheses used. $()$ refers to the direction of a plane, $\{ \}$ refers to a group (or family) of planes, $[]$ refers to a (general) direction and $\langle \rangle$ refers to a group of directions. The need for groups and families is due to the symmetry of the crystal lattice where multiple planes or direction describe the same structure but have different Miller indices when defined from the same reference coordinate system. For instance, it is evident from figure 2.2 that (100) , (010) and (001) correspond to the same crystal plane with regards to the structure and is thus part of the same $\{100\}$ family of crystal planes.

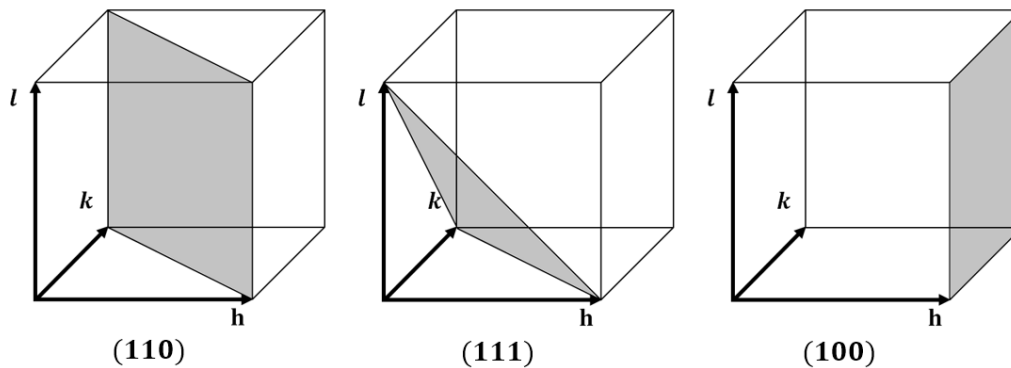


Figure 2.2: Three planes (colored) through a cubic lattice unit cell, described by their respective Miller indices (hkl) .

Euler angles

Though Miller indices are easy for humans to interpret it is not effectively employed in a computational setting, especially with regards to arbitrary orientations. Instead Euler angles can be used. The Euler angles, $(\varphi_1, \Phi, \varphi_2)$, are three angles that defines successive rotations, with which all possible orientations can be represented. However, it must be said that different conventions exist for what the angles represent. In this paper the Bunge convention (or the ZXZ convention) is used and is defined for a coordinate system (X, Y, Z) as follows:

1. A rotation φ_1 around Z , resulting in the new coordinate system (X', Y', Z')
2. A rotation Φ around X' , resulting in the new coordinate system (X'', Y'', Z'')
3. A rotation φ_2 around Z'' , resulting in the new coordinate system (X''', Y''', Z''')

The Euler angles are often used with regards to a known reference configuration.

2.2 Grain boundaries

Though small in width compared to the typical size of a grain, its effect on the system mechanics is often significant enough for it to be important to consider. The modern study of grain boundaries started in the mid 1900s when important developments in high-resolution electron microscopy were made available. Before this, the grain boundaries were assumed to be made up of an amorphous transition region acting as mortar between bricks [46], however this was found not to be the case. Instead the grain boundaries were found to be anisotropic, inconsistent with the previous assumptions. Still, however, after decades of research on the subjects, the description of this anisotropy is incomplete, at any length-scale, and thus a best-effort must be made.

In essence the grain boundary is created by the disorder between adjacent grains, as illustrated in figure 2.3, where two grains are rotated relative to each other by an angle θ , often referred to as the misorientation. However, the figure is idealized and only made to roughly illustrate the boundary without any deformation and with atoms that cross the grain boundary (GB) having been simply removed. A more thorough discussion on grain boundaries is found later in this chapter. In figure 2.3 it can be seen that at the grain boundary there is a reduction in the atom density and thus a higher diffusion rate is facilitated. It is also a place for other atoms to get “stuck” as is the case in segregation, a phenomena that is also discussed later on and which can have significant effect on the mechanical behavior of the material. From figure 2.3 it is evident that there are three regions to consider: the free surfaces, the grain boundary and the bulk. The diffusion coefficient is in general highest at free surfaces, lower along grain boundaries and lowest in the bulk, i.e. in the grain interiors.

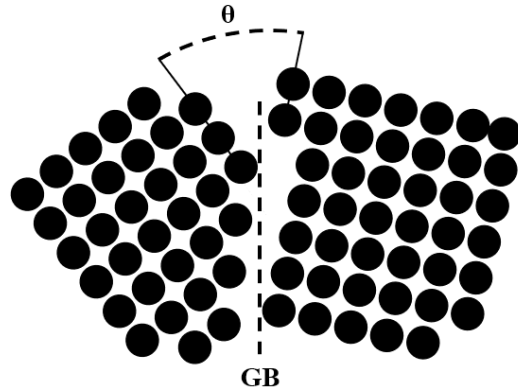


Figure 2.3: The formation of a grain boundary (GB) between two adjacent grains that are rotated by an angle θ relative to each other.

At some places, where three crystals are in contact, a triple junction is formed. As illustrated in figure 2.4. Again, just as figure 2.3, this is not a realistic distribution of the atoms. The fact remains, however, that there is a higher degree of disorder at a triple junction that facilitated even higher diffusion rates compared to the interface between two grains. However, as only 2D structures are considered in this work the triple junction is just a point, whereas for a 3D case it is a line, or a pipe, with a relatively high rate of diffusion. For this reason it is assumed to have a minimal effect in a 2D case and is thus not further considered in the present work.

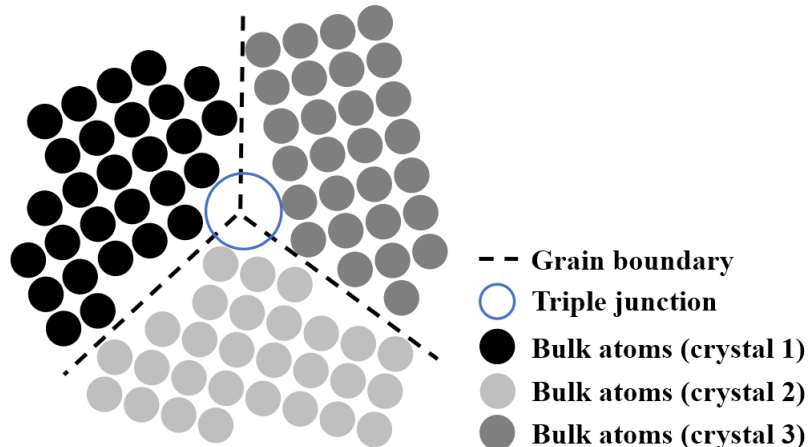


Figure 2.4: The formation of a triple junction between three adjacent grains that are rotated relative to each other.

2.2.1 Texture and grain boundary specification

The scalar misorientation, though convenient, is not sufficient to describe the entire character of a grain boundary. The misorientation is what could be called a geometrical, or macroscopic, degree of freedom and five such macroscopic degrees of freedom are usually required. These include the relative orientation of the grains (three degrees of freedom that together comprise the scalar misorientation θ) and the grain boundary plane orientation (two degrees of freedom). Furthermore an additional degree of freedom regarding the handedness of the grain might be needed for unsymmetrical lattices, but this does not need to be considered

in this paper which only deals with symmetrical crystal structures.

There is also the microscopic degrees of freedom, which are related to the offset between the two adjacent lattices at the grain boundary. Generally three degrees of freedom are needed. These are more difficult to take into consideration compared to the macroscopic degrees of freedom as they are connected to the relaxation at the boundary. The microscopic degrees of freedom will be omitted in this report.

In polycrystal samples one often refer to the “texture” of the material. The material’s texture will also influence the character of the grain boundaries in the polycrystal aggregate. If the orientations of the grains in a material with cubic crystal structure are completely random, it is said to have no texture and the variation of the misorientations would follow the so called Mackenzie distribution shown in figure 2.5 [35].

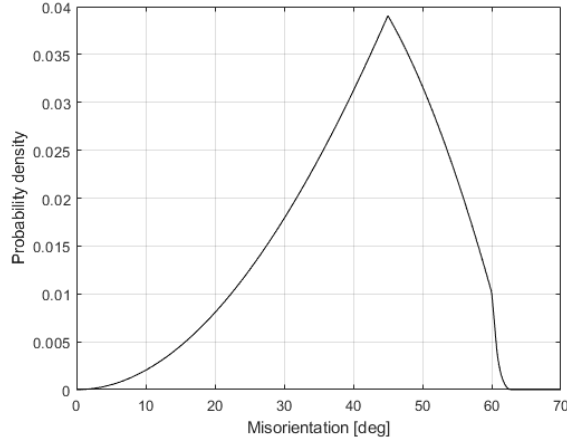


Figure 2.5: The Mackenzie distribution, describing the distribution of misorientations in a randomly textured polycrystal of cubic structure.

2.2.2 Tilt and twist, the decomposition of rotation

The total rotation across a grain boundary can be decomposed into two rotational components: a twist component and a tilt component. A twist is a rotation with the rotation vector parallel to the grain boundary normal. Consequently the tilt component is any rotation with the rotation vector perpendicular to the grain boundary normal. However, these operations do not commute. Thus depending on which order of operation is chosen, different rotation angles apply [54]. This formalism might be of interest as even though the misorientation between two pairs of grains may be identical, the associated diffusion rate might be different, depending on if the misorientation is due to a tilt or a twist rotation for which different structures, or misfit dislocations, are formed.

2.3 Transient diffusion described by Fick’s second law

In this paper the finite element method is used to calculate the transient diffusion in different microstructures. However, different methods can and have been used, such as finite differences and analytical solutions [62, 14, 58], of which many are based on Fick’s second law of mass diffusion, which describes time-dependent, transient diffusion. Fick’s second law is simply a combination of Fick’s first law,

$$\mathbf{J} = -D\nabla c \tag{2.1}$$

describing steady-state diffusion, where \mathbf{J} is the density flux, D is the diffusion coefficient and c is the concentration, and the continuity equation

$$\frac{\partial c}{\partial t} + \nabla \cdot \mathbf{J} = \sigma \quad (2.2)$$

which describes the conservation of mass, which holds true for pure diffusion (in contrast to a diffusion-reaction case) [36]. σ is a generation term. Combining equation 2.1 and 2.2 as well as choosing $\sigma = 0$, results in Fick's second law

$$\frac{\partial c}{\partial t} = D\Delta c \quad (2.3)$$

where $\Delta (= \nabla^2)$ is the Laplace operator.

2.3.1 Analytical solutions to Fick's second law

The solution to Fick's second law, equation 2.3, subjected to different boundary conditions under both steady-state and transient conditions, has been studied in depth analytically and is often used when measuring physical quantities in experiments, as discussed later in this chapter. Two of these analytical solutions is that of the thin-film solution and the constant source solution.

The thin-film solution

The thin-film solution is the solution to Fick's second law, equation 2.3, given as the concentration, $c(x, t)$, a distance x from the boundary at time t in a one dimensional (1D) beam occupying the half-space $0 < x < \infty$, with the initial condition

$$c(x, 0) = c_0\delta(x) \quad (2.4)$$

where c_0 is the amount of diffusing substance ("source" atoms per unit area) and δ is the Dirac delta function. The solution to this problem is given by

$$c(x, t) = \frac{c_0}{\sqrt{\pi Dt}} \exp\left(-\frac{x^2}{4Dt}\right) \quad (2.5)$$

and is often referred to as the heat kernel (heat conduction and diffusion is governed by the same equations) [10].

Constant source solution

With the aid of the heat kernel, equation 2.5, other solutions to different types of boundary conditions can be derived. Such as for a constant source, which can be viewed as multiple line sources stacked after one another in the half space, $-\infty < x \leq 0$. The solution to which is given by

$$c(x, t) = c_0 \operatorname{erfc}\left(\frac{x}{2\sqrt{Dt}}\right) \quad (2.6)$$

where erfc is the complementary error function [36].

2.4 Lattice diffusion

Most diffusion is fundamentally driven by Brownian motion and is chaotic and stochastic by nature. In a crystalline material, however, the motion is not as continuous as in a liquid or a gas but instead "jumps" between lattice sites, defining a so called jump frequency. As these jumps must overcome an activation energy, lattice diffusion is highly temperature dependent. This is discussed further in section 2.4.5.

Due to the aforementioned facts, two time scales exist, that of the (shorter) individual jumps described by thermal activation and that of (longer) multiple jumps that leads to a microscopic diffusion [36]. Furthermore,

diffusion is often, except for the direct interstitial mechanism described below, collective, where multiple lattice atoms are involved in the movement of the diffusant (a bulk atom or a precipitate/impurity). The different processes also occur simultaneously in most cases and translate to the macroscopically measured diffusion coefficient. The descriptions below are primarily for diffusion within the lattice, that is the individual grains, but the mechanisms are also related to those of grain boundaries, as will be discussed later in this chapter.

2.4.1 Interstitial diffusion mechanism

This mechanism is divided into two types: the direct and the indirect interstitial diffusion mechanism. The former is usually observed for relatively small diffusants, i.e. for diffusants of relatively smaller atom size, such as hydrogen in metal, but also heavier atoms, e.g. carbon and oxygen, can be grouped here. For these atoms the lattice is not required to deform in order for the diffusants to move from one site to another, in general resulting, in a higher diffusivity, or, in other words, a higher jump frequency [36]. This is one reason for the high rate of diffusion of hydrogen, as was discussed in chapter 1. This is illustrated in figure 2.6 for a general cubic lattice and the specifics do, as one can imagine, look different depending on the type of lattice, as they have different interstitial sites. But the principle remains the same.

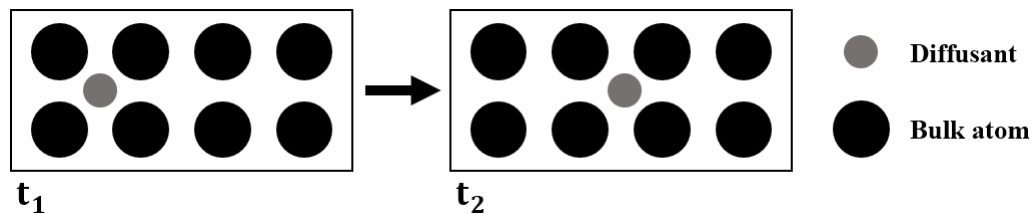


Figure 2.6: Diffusion by means of the direct interstitial mechanism where a smaller diffusant jump from one interstitial site, at time t_1 , to the next, at time t_2 .

For cases when the size of the diffusing atoms is similar, or equal, in size to that of the solvent atoms, diffusion can take place by the co-linear interstitialcy mechanism, an indirect interstitial mechanism. During this type of diffusion extra atoms participates in the movement of the solvent atoms, for which the atoms move in unison, as illustrated in figure 2.7. Thus, the atoms move in half-steps from a lattice site to an interstitial site. This type of diffusion is, however, rare in metals [36].

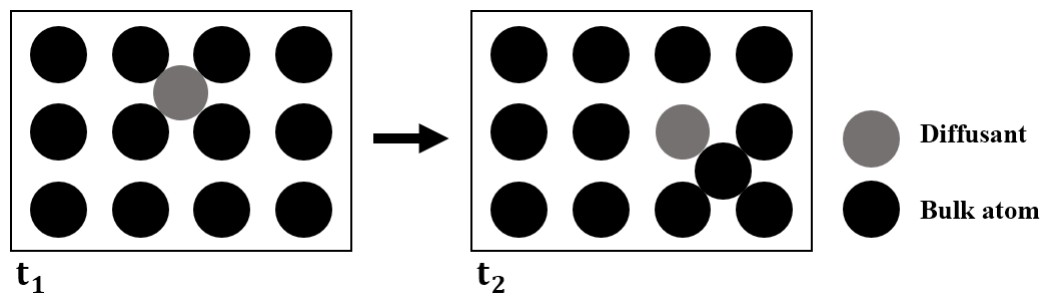


Figure 2.7: Diffusion by means of the indirect, co-linear, interstitial mechanism where a diffusant (that might be the same as the bulk atom or a precipitate) jumps from one interstitial site, at time t_1 , to a lattice site, at time t_2 .

2.4.2 Vacancy diffusion mechanism

As one might deduce, the vacancy mechanism is when a diffusant simply moves into a neighboring vacancy, as illustrated in figure 2.8. This also means that the vacancy will move in the opposite direction to the

diffusant. This can happen both for single vacancies and for multiple vacancies (divacancies, trivacancies and so on). The latter can be a result of the solvent's binding energy creating agglomerates of vacancies [36].

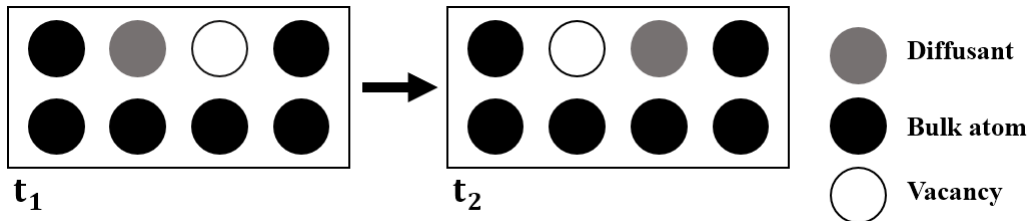


Figure 2.8: Diffusion by means of the vacancy mechanism where a diffusant moves into a neighboring vacancy, at time t_2 . Leading to the vacancy moving in the opposite direction relative to the diffusing atom.

2.4.3 Other diffusion mechanisms

Other mechanisms have also been identified, such as non-defect mechanisms. These are observed for larger diffusant atoms and are caused by a collective jump of two or more atoms. Firstly, there is the direct exchange where two atoms change places, which require large deformations. Secondly, there is the ring mechanism whereby multiple atoms are rotated and switch places as in a game of musical chairs, illustrated in figure 2.9. For the former case it would simply be an exchange between bulk atom 1 and the diffusant, from time t_1 to t_2 . However, it can be noted that these processes do not constitute the main diffusion mechanisms in solids, but are more common in amorphous materials [36].

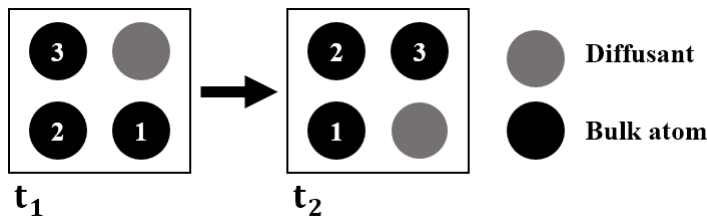


Figure 2.9: Diffusion by means of the ring mechanism where a diffusant moves together with bulk atom 1, 2 and 3 in unison, from time t_1 to time t_2 .

2.4.4 Externally applied forces

The previous sections dealt with the internal thermal diffusion processes caused by Brownian motion. In addition, however, diffusion can also be driven by external forces. This will just be a very brief introduction, as most things in this chapter, and just serves to give a birds eye view of the subject and to form connections between the large-scale observations and what is happening on an atomic scale.

External force can be due to, for example, mechanical stress, under which the creation and movement of dislocations facilitates diffusion. Furthermore, diffusion can be electrically induced, resulting in so-called electromigration by which the electric current induces two forces: The first is the electrostatic force imposed onto the charged ions. However, as the ions are surrounded by electrons, and thus somewhat shielded, it is rather the second effect that cause electromigration, namely the momentum transferred from the conduction electrons to the ions. If the transferred energy exceeds the activation energy, diffusion will likely occur, in the direction of the current [34]. As electromigration is related to the activation energy of diffusion, it will vary depending on the species and/or location (e.g. in the lattice or along a grain boundary).

2.4.5 Temperature dependence of diffusion described by the Arrhenius relation

As was mentioned in the introduction to this section, diffusion is temperature dependent. In many cases this dependence has been found to agree with the so called Arrhenius equation

$$D = D_0 \exp\left(-\frac{Q}{RT}\right) \quad (2.7)$$

where D_0 is a constant, Q is the activation enthalpy, R is the gas constant and T the temperature. In some cases, involving multiple diffusion processes, a relation is found to be the sum of multiple such expressions [36].

2.5 Grain boundary diffusion

Now that the structure of the grains and how material in them flow has been discussed, it is time to further continue the discussion regarding grain boundaries, from the brief mentions that has been made. It was mentioned previously that before the 1950s, a grain boundary was thought to be an amorphous region. This turned out not to be the case. However, a grain boundary is not strictly ordered either, but takes the form of a quasi-crystalline structure with some degree of periodicity [46]. The way the grain boundary is modeled in the simulations in the present work is described in chapter 3 and 4, while this chapter deals with the general properties, as well as specific experimental observations that is the basis of those models. But first the already mentioned misorientation is defined.

2.5.1 Misorientation and disorientation

The structure of the grain boundary depends on the relative orientation of the two adjacent crystals, resulting in various degrees of order and disorder. Considering a system as the one shown in figure 2.10, where the orientation of each grain is described by the rotation matrices \mathbf{g}_1 and \mathbf{g}_2 , relative to a reference configuration. Then the mapping from the first grain to the other can be calculated as

$$\mathbf{g}_2 = \mathbf{g}_{12}\mathbf{g}_1 \quad (2.8)$$

where \mathbf{g}_{12} is a transformation matrix and

$$\mathbf{g}_{12} = \mathbf{g}_2\mathbf{g}_1^{-1} = \mathbf{g}_2\mathbf{g}_1^T \quad (2.9)$$

As a rotation matrix is orthogonal, $\mathbf{g}_1^{-1} = \mathbf{g}_1^T$ and equation 2.9 holds true. The scalar rotation angle between the grains, called the misorientation, is defined by the rotation matrix \mathbf{g}_{12} and can be calculated as

$$\theta = \arccos\left(\frac{\text{tr}(\mathbf{g}_{12}) - 1}{2}\right) \quad (2.10)$$

However, as there might exist symmetries for the unit cell, as it does for a cubic unit cell, there might exist a smaller rotation that yield the same structure. This can be taken into account by applying a symmetry operator, \mathbf{O}_s , that is a member of the symmetry group \mathcal{O} , to the misorientation matrix \mathbf{g}_{12} . As there are multiple symmetry operators they must all be tested. The smallest angle obtained is taken as the misorientation, according to

$$\theta = \min_{\mathbf{O}_s \in \mathcal{O}} \left| \arccos\left(\frac{\text{tr}(\mathbf{O}_s\mathbf{g}_{12}) - 1}{2}\right) \right| \quad (2.11)$$

The symmetry conditions can be taken further by also including switching symmetries by considering both \mathbf{g}_{12} and \mathbf{g}_{21} in equation 2.11, resulting, for the smallest angle obtained, in what is known as the disorientation.

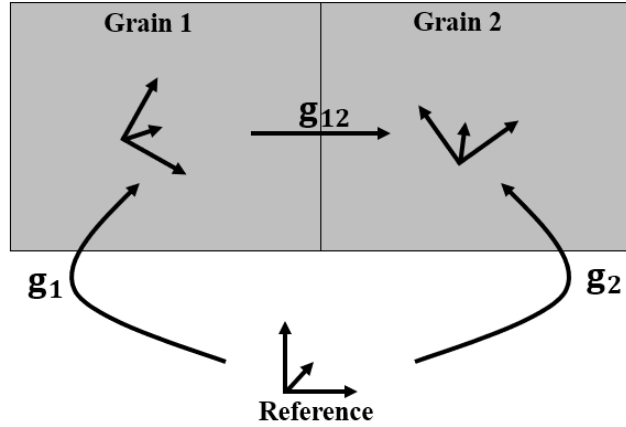


Figure 2.10: Two grains with different orientations relative to a reference configuration, described by the rotation matrices \mathbf{g}_1 , \mathbf{g}_2 and \mathbf{g}_{12} .

2.5.2 Grain boundary interfaces

Because of the symmetric nature of lattices with regards to rotation, the interface at the grain boundary is not simply two distinct crystals in contact with each other, but, depending on the orientation, might form special types of interfaces. In the next chapter the concept of the coincident site lattice (CSL) is considered as a mathematical tool to categorize some of these special boundaries. In this chapter, however, only some special cases that will yield lower interfacial energy compared to an general interface is considered. Basically there are three types of interfaces: coherent, semi-coherent, and incoherent. All three refer to some boundary plane symmetry, where a coherent boundary has a perfect symmetry matching between planes and an incoherent boundary have no symmetry. Not surprising, a semi-coherent boundary has some intermediate degree of symmetry matching.

As an example, a coherent twin boundary is considered. Such a boundary arise when the periodicity, or structure, at the interface matches, as illustrated in figure 2.11, for a misorientation angle of θ . The interface does not contain any misfit dislocations and therefore has a low interfacial energy. Even if there is a slight mismatch in the lattice periodicity at the interface, it can still be considered coherent as long as no defects are introduced. If the coherency is not perfect, either because of an unsymmetrical tilt or due to the grains having different lattice constants, misfit strains will be introduced in the structure [46].

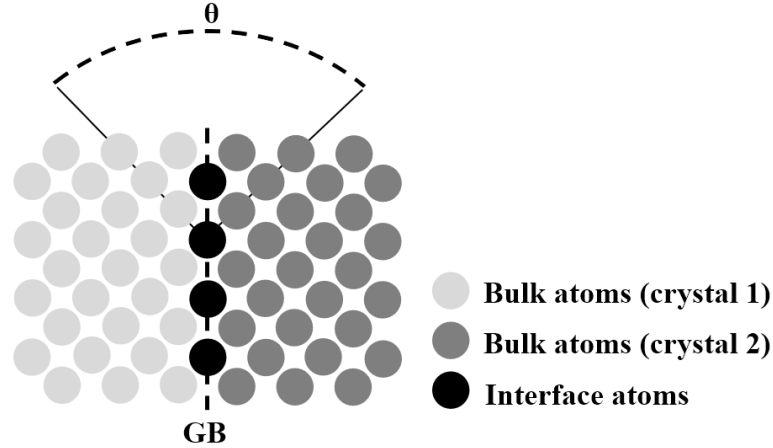


Figure 2.11: A coherent twin grain boundary (GB) where the disorientation angle θ , between crystals 1 and 2, results in a perfect match at the grain boundary interface.

If there still is some, but not equal, periodicity at the boundary some dislocations will be introduced. This is known as a semi-coherent boundary (that is no longer a twin boundary). It is these cases, as will be discussed in the next chapter, that the CSL theory tries to handle.

2.5.3 Segregation

Grain boundaries facilitate what is known as segregation, a local enrichment of impurities which is sometimes categorized as either equilibrium or non-equilibrium segregation. The former refers to processes that, not surprisingly, takes place in equilibrated systems and that are not governed by the system's history but are instead driven by a minimization of energy. This will lead to an increase in segregation of impurities along grain boundaries and free surfaces because of the existence of excess volume (higher volume compared to the lattice) at these sites, resulting in a reduction of the interfacial energy. The second type of segregation occurs during rapid changes in the system, such as a temperature changes during quenching, and depends on the processing history [46].

The degree of segregation is given by the segregation factor $s \leq 1$ and is unity for self-diffusion. There are a multitude of models to quantify the segregation factor and has in some cases been found to follow that of the Arrhenius equation [7]. The segregation parameter is often found in the triple product $s\delta D_{GB}$, where δ is the grain boundary width and D_{GB} the grain boundary diffusion coefficient. This is important as some experimental conditions only allow for measurements of the triple product, not the parameters individually. As the segregation is not the main interest in this work and only used when comparing experimental results, it is not discussed further, but are still included in some equations for completeness.

2.6 The Fisher model, an analytical approach to grain boundary diffusion

The earliest analytical study of grain boundary diffusion is that of Fisher [14] and combined with the aforementioned advances in measuring devices, is the main seeds of the academic field of grain boundary diffusion.

In Fisher's model the grain boundary is modeled as a slab of width δ between two crystals, as shown in figure 2.12, and where there is two different diffusion coefficients, D_v and D_{GB} , for the bulk (volume) and the grain boundary, respectively, and where $D_v < D_{GB}$. The diffusants are introduced at the free surface ($y = 0$) and is in Fisher's calculations considered as a constant source that is raised from zero to unity at time $t = 0$. Fisher's solution yields the concentration profile as a function of the diffusion coefficients, δ and

time. Bicrystal experiments can therefore be compared to this theoretically derived concentration profile, in order to extract the grain boundary diffusion coefficient.

Other boundary conditions have been considered, such as the commonly used result by Suzuoka for an instantaneous source [55]. However, it must be noted that Fisher's solution, and subsequent analytical studies, does not directly consider the microstructure. Furthermore, Fisher's solution is not used in practice as it is considered to be incorrect. As an alternative the more recent solution by Whipple is commonly used [58].

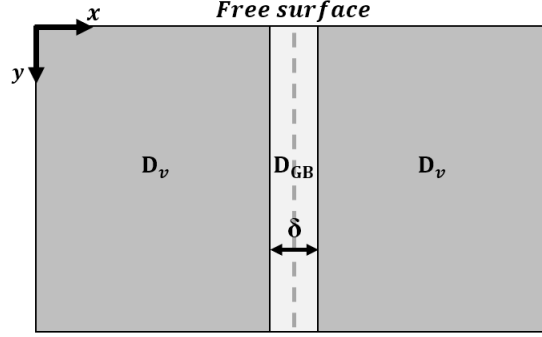


Figure 2.12: The Fisher model for grain boundary diffusion with a grain boundary of width δ and diffusion coefficient D_{GB} , inlaid between two crystals with diffusion coefficient D_v .

2.6.1 Whipple's solution

Whipple's solution is considered more correct than that of Fisher and is explicitly given by

$$c = \operatorname{erfc} \frac{\eta}{2} + \frac{\eta}{2\sqrt{\pi}} \int_1^{\Delta} \frac{1}{\sigma^{3/2}} \exp\left(-\frac{\eta^2}{4\sigma}\right) \operatorname{erfc}\left(\frac{1}{2}\sqrt{\frac{\Delta-1}{\Delta-\sigma}}\left(\frac{\sigma-1}{\beta} + \xi\right)\right) d\sigma \quad (2.12)$$

where c is the concentration, σ is the integration variable and ξ , η , β and Δ are dimensionless variables given by

$$\xi = \frac{x-a}{\sqrt{D_v t}}, \quad \eta = \frac{y}{\sqrt{D_v t}}, \quad \beta = \left(\frac{D_{GB}}{D_v} - 1\right) \frac{a}{\sqrt{D_v t}}, \quad \Delta = \frac{D_{GB}}{D_v} \quad (2.13)$$

and where $a = \delta/2$ (half the grain boundary width).

However, the practical significance of the analytical solutions, in regards to natural polycrystals, is small, as pointed out by Herzig and Mishin [22], as they are mathematically complex and not easily transferable to complex geometries. That is of course where numerical models such as the finite element method provide greater flexibility.

2.6.2 The extended Fisher model and Harrison A, B and C diffusion kinetics regimes

The Fisher model can be extended to include multiple parallel grain boundaries, as shown in figure 2.13, where the grain boundaries are pairwise separated by a distance d . The solutions to such diffusion scenarios can be classified according to the Harrison A, B and C kinetics regimes [20]. With regards to this classification, the penetration depth l is of interest and is given by \sqrt{Dt} , where D is the diffusion coefficient describing the diffusion process and t is the duration of the diffusion process. Depending on the state of the system, A, B or C kinetics regimes can be distinguished. These classifications become useful when discussing the validity of experimental methods and the conclusions derived from them.

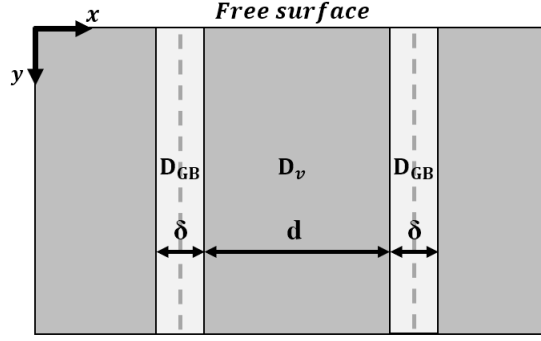


Figure 2.13: A Fisher-like polycrystalline model for grain boundary diffusion with grain boundaries of width δ and diffusion coefficient D_{GB} , inlaid between crystals with bulk diffusion coefficient D_v . The grain boundaries are pairwise separated by a distance d .

Examples of the A, B and C regimes for the Fisher-like polycrystal model, are shown in figure 2.14 and their differences are discussed below. In figure 2.14, the border of the darker region can be seen as a concentration contour of a diffusing substance. The penetration depth of the three kinetic types are defined by the different diffusion coefficients discussed in the following sections. In the transition region between one kinetic region to the next, the kinetic specific theories are often ill defined and not usable.

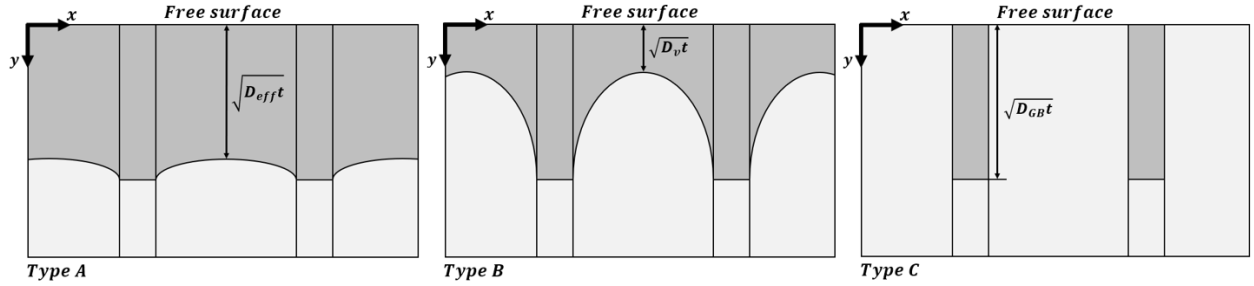


Figure 2.14: Examples of Harrison's type A, B and C kinetics regimes for some diffusing substance introduced at the free surface. The borders between the light- and dark-gray regions can be seen as a contour line defined for some concentration. These are, however, only sketches and the contours are not mathematically correct.

Type A

For type A kinetics the diffusivity in the bulk is relatively high compared to the grain size, more specifically $\sqrt{D_v t} \gg d$ and/or the diffusivity in the grain boundary is not much higher than that of the bulk (observed at high temperatures) and/or long diffusion times can be assumed [22]. This means that the contour lines of the concentration in the grains will overlap and the system can be defined by a single effective diffusion coefficient, in [20] found as

$$D_{eff} = fD_{GB} + (1 - f)D_v \quad (2.14)$$

where f is the ratio of grain boundary volume to the total volume of the polycrystal under consideration.

Type B

For type B kinetics it holds that $s\delta \ll \sqrt{D_v t} \ll d$, where s is the segregation factor. The grains can therefore be considered as isolated from each other and thus the solution for a single crystal is still valid in these cases [22].

Type C

In the case of type C kinetics the bulk diffusivity is negligible and practically all diffusion occurs along the grain boundary. In this case $\sqrt{D_v t} \ll s\delta$ [22].

2.7 Experimental methods for measuring the diffusion coefficient

In order to compare analytical and/or simulated results with those of experimental investigations, it can be a good idea to understand how those have been obtained. When it comes to experimental methods for diffusion measurements they can, according to Mehrer [36], be grouped into two categories: the direct methods, discussed in this paper, where Fick's law is directly observed in terms of the long-range diffusion and the indirect methods, where the individual jumps of atoms are studied. The latter will not be discussed here but is described in Mehrer [36]. For the discussions related to experiments, the Harrison classifications will come in handy as, depending on the prevailing kinetics, some restrictions on what can be measured might exist

One of the most widely used direct methods is that of radiotracer diffusion, described below. Some of the quantitative measurements that can be made, for example by means of the radiotracer method, are described by Peterson [45] and can be summarized as:

- The penetration depth, for some specified concentration, along the grain boundary.
- The angular difference between the grain boundary and the concentration contour.
- The total amount of diffused substance at some specified penetration depth.

2.7.1 Radiotracer diffusion and the serial sectioning method

In radiotracer diffusion experiments a radioactive isotope is used as the diffusant and work both for impurity- and self-diffusion, where the activity will be proportional to the concentration of the isotopes. The diffusant is deposited on the free surface of the specimen, which is annealed to initiate diffusion [36]. The next step is to measure the concentration field, which can be achieved in a multitude of ways, however, only the serial sectioning method is considered here, because of its wide use.

The serial sectioning method is a method whereby the radioactivity is measured in planes parallel to the free surface. Which yield the relative concentration as a function of the penetration depth, as shown in figure 2.15. Although the proportionality constant is often unknown, the diffusivity can in some cases be figured out from the shape of the penetration profile.

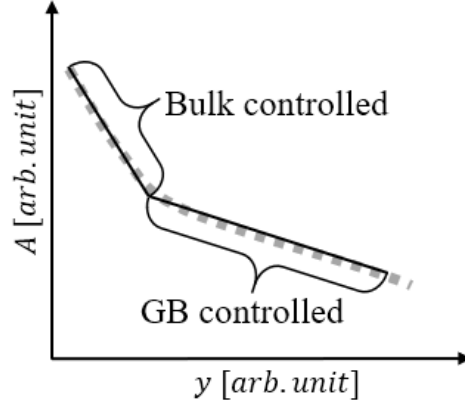


Figure 2.15: An example of the measured radioactivity A as a function of the penetration depth y . Two distinct regions are observed, where the grain boundary (GB) controlled region, or tail region as it is often referred to, is predominantly described by the grain boundary diffusion and the left-most region by the bulk diffusion.

This method does not generally differentiate between the bulk and the grain boundary as the total radioactivity in a slice is measured. However, depending on the kinetic regime, discussed in previous section, methods have been devised to extract system parameters from penetration profiles and are discussed below. However, because it is not always known from the start of an experiment which kinetic region prevails, and thus which assumptions that are appropriate, the conditions must be tested and verified for the derived values.

Type A

If the system obeys type A kinetics the penetration profile will not have two distinct regions as shown in figure 2.15, but rather overlap to a continuous line described by both the bulk- and grain-boundary diffusion, expressed as an effective diffusion given by equation 2.14. In this regime the penetration profile will follow that of ordinary solutions derived for volume diffusion. For a constant source, this is given by equation 2.6 and the measured concentration (or radioactive activity) will be proportional to $\text{erfc}(y/2\sqrt{D_{eff}t})$. Though D_{eff} can be calculated, δ is still needed, as well as D_v , to calculate D_{GB} according to equation 2.14.

Type B

For B type diffusion two distinct regions, as shown in figure 2.15, are observed. For this regime, in the case of a bicrystal of Fisher-type and under the assumption of Whipple's solution being correct, the theory of Le Claire can be used [32]. According to Le Claire, the observation that if the logarithm of the concentration is plotted against $y^{6/5}$, as proposed by Levine and MacCallum [33] and where y is the penetration depth beneath the surface, a straight line will be obtained in the grain boundary dominated tail region. From its slope the triple product $s\delta D_{GB}$, where s is the segregation factor, can be determined by

$$s\delta D_{GB} = 1.322\sqrt{\frac{D_v}{t}} \left(-\frac{\partial c}{\partial y^{6/5}} \right)^{5/3} \quad (2.15)$$

for a constant source [32]. The validity of equation 2.15 is restricted by two parameters α and β (not the same β as defined by Whipple in in equation 2.13) these are defined as

$$\alpha = \frac{s\delta}{2\sqrt{D_v t}}, \quad \beta = \frac{s\delta D_{GB}}{2D_v\sqrt{D_v t}} \quad (2.16)$$

Equation 2.15 is valid for $\alpha < 0.1$ and $\beta > 10$ [38]. This is compliant with the conditions of type B diffusion discussed in previous section. It is evident that if δ and s is unknown, then D_{GB} can not be determined merely by equation 2.15 and additional methods are required. However, in some cases the assumption $\delta = 0.5\text{nm}$, made by Fisher [14], is often used.

Though equation 2.15 was derived for a bicrystal the solution should be valid for a polycrystal as the grain boundaries are considered isolated from each other under type B kinetic conditions [38], as discussed in section 2.6.2.

Type C

If the system obeys type C diffusion kinetics, the grain boundary diffusion coefficient can be measured directly, since effectively no diffusion takes place in the bulk [20]. In this case equation 2.6 can once again be utilized, using D_{GB} . Thus the concentration will be proportional to $\text{erfc}(y/2\sqrt{D_{GB}t})$.

Chapter 3

Grain orientation dependent diffusion

The rate of diffusion is dependent on the relative orientations of the grains, as well as the inclination of the grain boundary plane, as different types of boundaries (coherent, semi-coherent etc.) might be produced. However, as no complete theory exists to describe the diffusion coefficient as a function of misorientation, let alone of grain boundary inclination, some well established results related to grain boundary energy will be utilised in order to derive such a model.

The energy of the grain boundary will be discussed first. Though not all of the theory will be utilised, it serves to understand the origin of the grain boundary energy. This is followed by a discussion on the relationship between grain boundary (excess) energy and excess volume. The latter is then used to form the grain boundary diffusion model proposed in this work. Lastly, the proposed model is compared to available experimental data.

3.1 Grain boundary energy

In this section only the grain boundary energy will be discussed. However, as noted in the introduction to this chapter, this will be useful when later on a model for the diffusion coefficient is proposed.

3.1.1 The dislocation model

Though initially developed for low angle grain boundaries, the dislocation model have, quite unexpectedly, been proven to be useful also for other grain boundary types. The dislocation model considers arrays of dislocations that are introduced for low angle boundaries, as illustrated in figure 3.1. Other, more complex, dislocation distributions have been suggested to better explain, for instance, stress fields in the vicinity of grain boundaries. These are not discussed here but can be found in, for example, Sutton and Balluffi [54].

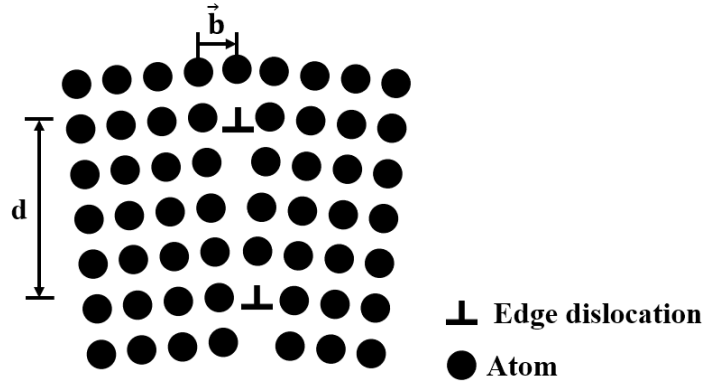


Figure 3.1: Edge dislocations, defined by the Burgers vector \vec{b} , along a low angle symmetrical grain boundary separated by a distance d .

3.1.2 The Read–Shockley relation

Read and Shockley studied grain boundary energy of primarily low-angle grain boundaries using the dislocation model, where the energy required to introduce a dislocation into a lattice is considered. Thus they considered a wall of edge dislocations with a spacing d between dislocations, similar to that of figure 3.1. The distance d is related to the misorientation angle θ by means of the magnitude b of the Burgers vector \mathbf{b} , according to

$$d = \frac{b}{\sin \theta} \approx \frac{b}{\theta} \quad (3.1)$$

where the approximation $\sin \theta \approx \theta$ holds true for small angles [49]. The maximum angle for which this holds true is often set to 15° , as the dislocations cores will start to overlap for higher angles [24].

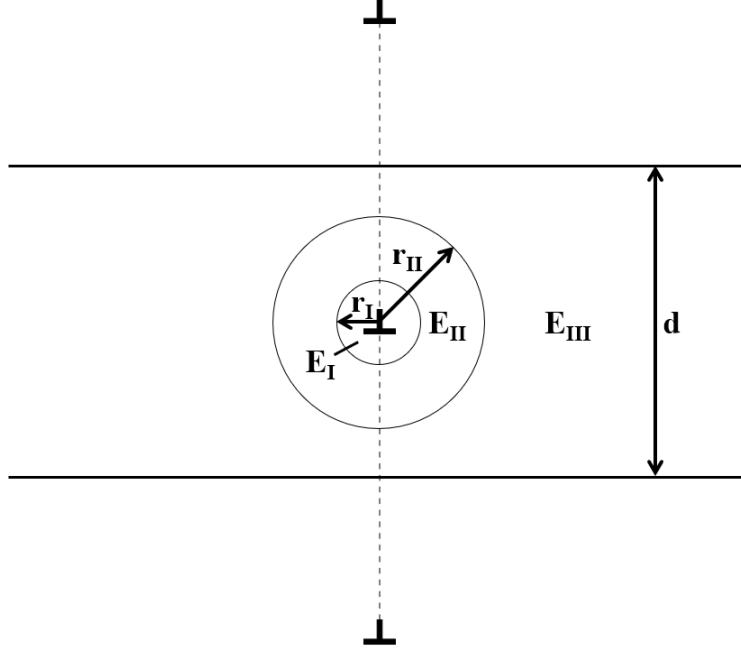


Figure 3.2: An array of dislocations spaced by a distance d . E_I and r_I denote the dislocation core energy and radius, respectively, E_{II} is the energy of the region between radius r_I and r_{II} and E_{III} is the energy of the region outside the radius r_{II} and confined to the region inside the strip of width d .

In order to calculate the grain boundary energy, the model, proposed by Read [49], and illustrated in figure 3.2, is used. Here $r_{II} = \mu d \gg r_I$ with $\mu \leq 1$ being a scaling factor. The total energy of the infinitely long strip is denoted E_s and can be evaluated from $E_s = E_I + E_{II} + E_{III}$. The core energy is denoted by E_I and the sum $E_{II} + E_{III}$ represents the elastic strain energy. In order to find E_s , a small change in misorientation angle, $\Delta\theta$, is considered. According to equation 3.1 this provides a change Δd in the dislocation spacing d according to

$$d + \Delta d = \frac{b}{\theta + \Delta\theta} \Leftrightarrow \frac{d + \Delta d}{d} = \frac{\frac{b}{d}}{\theta + \Delta\theta} \Leftrightarrow 1 + \frac{\Delta d}{d} = \frac{\theta}{\theta + \Delta\theta} = \frac{1}{1 + \frac{\Delta\theta}{\theta}} \quad (3.2)$$

This can be written as,

$$\left(1 + \frac{\Delta d}{d}\right) \left(1 + \frac{\Delta\theta}{\theta}\right) = 1 + \frac{\Delta d}{d} + \frac{\Delta\theta}{\theta} + \frac{\Delta d}{d} \frac{\Delta\theta}{\theta} = 1 \quad (3.3)$$

Because a small change in the misorientation angle is considered, the term $(\Delta d/d)(\Delta\theta/\theta)$ can be ignored, which results in the condition

$$-\frac{\Delta\theta}{\theta} = \frac{\Delta d}{d} = \frac{\Delta r_{II}}{r_{II}} \quad (3.4)$$

where the condition $r_{II} = \mu d$ have been used. The changes $\Delta\theta$ or Δd will result in a change in the energy E_s . However, only ΔE_{II} must be considered. This follows from that for a large enough values of the distance d , $\Delta E_I \approx 0$ and though the volume of region *III* increases, the elastic energy density decreases proportionally whereby the latter two cancel out [54]. Thus $\Delta E_s = \Delta E_{II}$. The elastic energy density of region *II* does not change, compared to region *III*, as it can be assumed to only to be affected by the enclosed dislocation. The area do, however, change. To find the energy of the expanded area, the work needed to form the dislocation

by shearing the lattice is considered. The work done is half the shearing force $\tau\Delta r_{II}$ multiplied by the distance moved, given by the length of the Burgers vector b . The shearing stress is given by

$$\tau = \tau_0 \frac{b}{r} \quad (3.5)$$

where $\tau_0 = G/2\pi(1 - \nu)$ for an edge dislocation [50] and where G is the shear modulus, ν is Poisson's ratio and r is the distance from the dislocation center. Thus the total work is given by

$$\Delta E_s = \frac{1}{2}\tau b\Delta r_{II} = \frac{\tau_0 b^2}{2r_{II}}\Delta r_{II} \quad (3.6)$$

Using equation 3.4 this can be written with respect to θ as

$$\Delta E_s = -\frac{\tau_0 b^2}{2\theta}\Delta\theta \quad (3.7)$$

Integration of equation 3.7 yields

$$E_s = \frac{\tau_0 b^2}{2}(A - \ln\theta) \quad (3.8)$$

where $A = 1 + \ln(b/2\pi r_I)$ when the boundary is along a crystal axis [50]. This is often written as $A = 1 + \ln(\theta_m)$, where θ_m denotes the maximum misorientation angle [49].

As equation 3.8 only represents the energy of a single dislocation, it must be divided by the dislocation density, $d = b/\theta$, to give the energy E per unit area. This provides the well known Read–Shockley equation

$$E = \frac{E_s}{d} = \frac{E_s\theta}{b} = \frac{\tau_0 b}{2}\theta(A - \ln\theta) = E_0\theta(A - \ln\theta) \quad (3.9)$$

It can be noted that the derivation of equation 3.9 assumes that the dislocations are uniformly spaced and that it only occurs for some specific misorientation angle. The deviation from equation 3.9 due to such considerations is small and can often be ignored [54].

For misorientation angles greater than θ_m the boundary can, as an assumption, be considered as an incoherent boundary with a constant grain boundary energy $E_m = E_0\theta_m$ [49]. Using this assumption allows equation 3.9 can to be written as

$$E_{RS}(\theta) = \begin{cases} E_m \frac{\theta}{\theta_m} \left(1 - \ln \frac{\theta}{\theta_m}\right) & \text{if } \theta < \theta_m \\ E_m & \text{if } \theta \geq \theta_m \end{cases} \quad (3.10)$$

where it has been used that $A - \ln(\theta) = 1 + \ln(\theta_m) - \ln(\theta) = 1 - (\ln(\theta) - \ln(\theta_m)) = 1 - \ln(\theta/\theta_m)$.

3.1.3 Coincident site lattice (CSL)

The previous assumption of incoherent boundaries for $\theta \geq \theta_m$ does not take the observed effects of reduced grain boundary energy at some specific misorientation angles into account. This observation indicates that there also exists some degree of coherency at the boundary at greater misorientation angles. These are often explained by so called coincident site lattices, or CSLs.

Coincident site lattices, or as Priester [46] rightfully suggested: ‘‘coincidence lattices’’, represent grain boundary configurations for which there is a good match, or periodicity, between lattice points on some lattice plane. However, these are just mathematical points and not necessarily actual common lattice sites at the grain boundary. The idea of the CSL stem from the observation that if a mathematical lattice is rotated, new larger unit cells can be defined which leads to a greater probability of a good fit between the lattices of the neighboring grains. The CSLs are usually described in terms of their Σ values which are calculated according to

$$\Sigma = \frac{\text{Coincidence unit cell volume}}{\text{Primitive unit cell volume}} \quad (3.11)$$

and is simply the area difference of the unit cells. This means that the CSL with $\Sigma = 5$ has a coincident unit cell five times larger than the lattice unit cell. Figure 3.3 illustrates a rotation of 36.86° around the $[100]$ axis, giving $\Sigma = 5$. Figure 3.4 shows a rotation of 38.21° around the $[111]$ axis, which gives $\Sigma = 7$ and figure 3.5 illustrates a rotation of 38.94° around the $[110]$ axis, which gives $\Sigma = 9$.

Though low Σ values generally result in lower energy grain boundaries, there is no reciprocal relationship between the Σ value and the energy and Σ -based models often fail in characterizing special (semi-coherent) boundaries [46, 59]. The grain boundary energy depends not only on the specific material but also on the relative twist and tilt, coherency, etc.

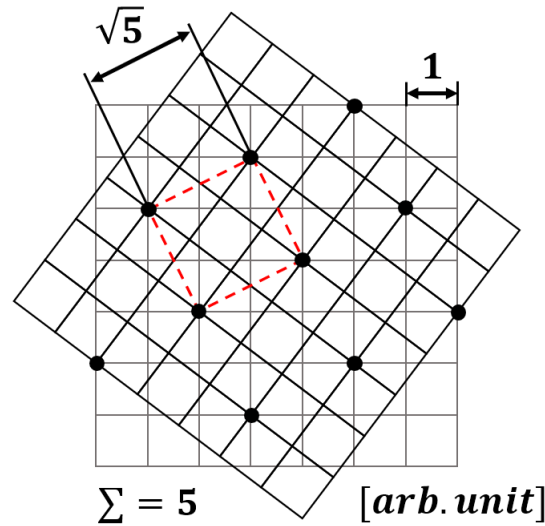


Figure 3.3: The $\Sigma = 5$ coincident site lattice, where a relative rotation of 36.86° around the $[100]$ axis has been made. The red square indicate the coincident unit cell.

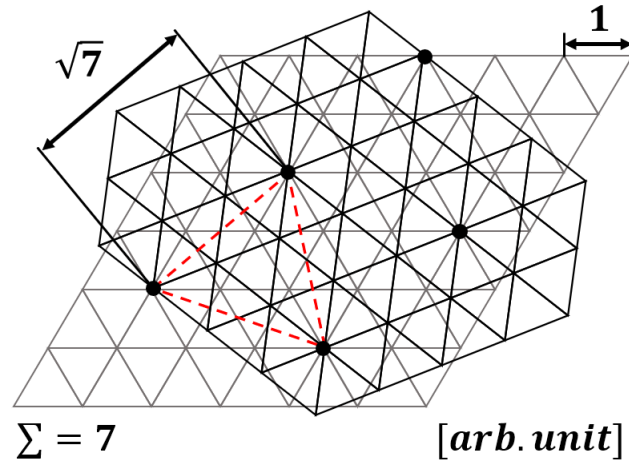


Figure 3.4: The $\Sigma = 7$ coincident site lattice, where a relative rotation of 38.21° around the $[111]$ axis has been made. The red triangle indicate the coincident unit cell.

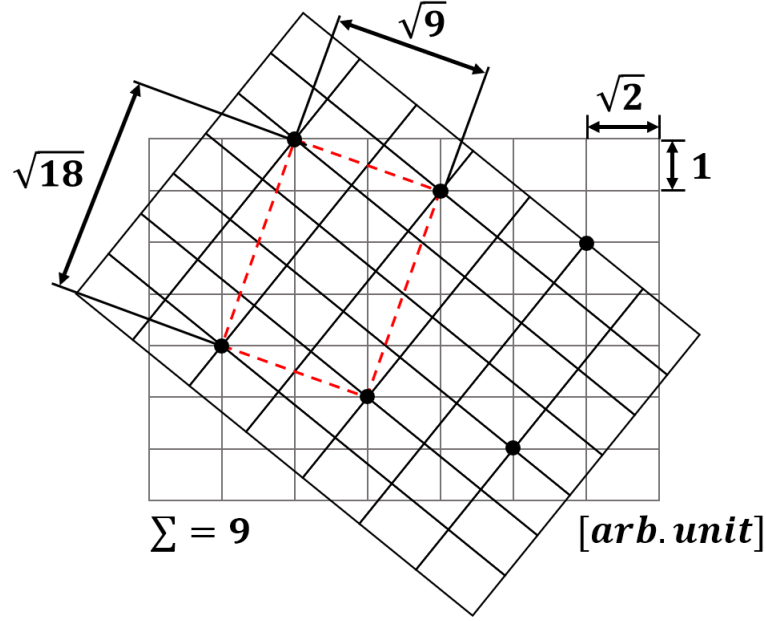


Figure 3.5: The $\Sigma = 9$ coincident site lattice, where a relative rotation of 38.94° around the $[110]$ axis has been made. The red square indicate the coincident unit cell.

3.1.4 The Brandon criteria

The CSL conditions yield exact angles. However, misorientations close to the CSL cases are also likely to yield lower boundary energy compared to an incoherent boundary and can be considered to have special properties, that must be accounted for. To identify near-CSL boundaries, a criterion that can be used to quantify the allowed variation $\Delta\theta$ can be stated as

$$\Delta\theta_{max} = \theta_0 \Sigma^{-n} \quad (3.12)$$

where θ_0 and n are variables describing different conditions [6]. Σ refers to the CSL Σ -value and an allowed range, $1 \leq \Sigma \leq \Sigma_{max}$, is often used. This extension of the CSL theory was introduced by Brandon [6], representing small deviations from the ideal CSL-cases by arrays of dislocation and where the values $\theta_0 = 15^\circ$, $n = 1/2$ and $\Sigma_{max} = 25$ were used. With these specific values, introduced by Brandon [6], equation 3.12 is usually referred to as the Brandon criteria. However, different values for θ_0 and n have been suggested and some have been summarized by Shekhar and King [27]. As for the general CSL theory, this is still an approximate approach, and a truly coherent and general model or theory for describing the grain boundary energy dependence on the five macroscopic parameters is still lacking.

3.1.5 Read–Shockley relation with CSL consideration

On the basis of the presented theory there appears to be at least some additional merit in adding the effect of CSLs to the Read–Shockley relation. It must be stated, however, that this CSL-methodology is not sufficient in describing a true grain boundary as only three out of the five characterizing parameters are accounted for, the influence of the grain boundary plane inclination is still neglected by this approach. Nonetheless it is this method has been employed in multiple studies, for example [17, 21]. The grain boundary energy reduction due to the CSLs can, following [21], be expressed as

$$E_\Sigma(\theta) = \begin{cases} -\frac{\hat{E}_m}{\Sigma} \left[1 - \frac{\Delta\theta}{\Delta\theta_\Sigma} \left(1 - \ln \frac{\Delta\theta}{\Delta\theta_\Sigma} \right) \right] & \text{if } \Delta\theta < \Delta\theta_\Sigma \\ 0 & \text{if } \Delta\theta \geq \Delta\theta_\Sigma \end{cases} \quad (3.13)$$

where $\Delta\theta$ is the deviation from the perfect CSL case, $\Delta\theta_\Sigma$ is the maximum deviation for which the CSL has an impact and \hat{E}_m/Σ is the energy reduction for an ideal CSL misorientation. Often \hat{E}_m is set to E_m . From equation 3.13 it is evident from this model that the lowest energy will be obtained for the lowest Σ value, which is mostly, although not generally, true. Adding equations 3.10 and 3.13 yields an expression for the total grain boundary energy according to $E(\theta) = E_{RS}(\theta) + E_\Sigma(\theta)$.

3.1.6 An interpolation approach, taking all five macroscopic degrees of freedom into consideration

The former models only take three degrees of freedom into consideration in terms of the misorientation. Which as mentioned previously is a simplification. Furthermore, the two parameters representing the grain boundary plane normal are not accounted for. An attempt to describe the energy as a function of all the five macroscopic degrees of freedom was made by Bulatov et al. [8]. They derived an energy function for FCC metals that is based on simulated results and using interpolation where the energies are unknown. In [8], the model was validated for four FCC materials (Al, Ni, Au and Cu). However, this should be valid for other FCC metals as the orientation dependence of the energy has been found to be scalable between different materials [43]. The function has been made available as a Matlab file by the authors and the model has been used for level set-based simulation of grain growth with anisotropic grain boundary energy by Hallberg and Bulatov [18].

A comparison between the model by Bulatov et al. [8] and that of the Read-Shockley relation, with CSL conditions, equation 3.13, is shown in figure 3.6. It can be seen that for low misorientation angles there is good correlation, although not for larger angles. It is emphasized that this version of the Read-Shockley equation has not been modified to work well with larger misorientations, though proposed modification exist, such as in [60], so this fact may not be surprising. Lastly, in the case of the model by Bulatov et al., only the major pit is included. However, the fact that the grain boundary orientation is taken into account by the model by Bulatov et al., probably more than makes up for the lack of the smaller pits.

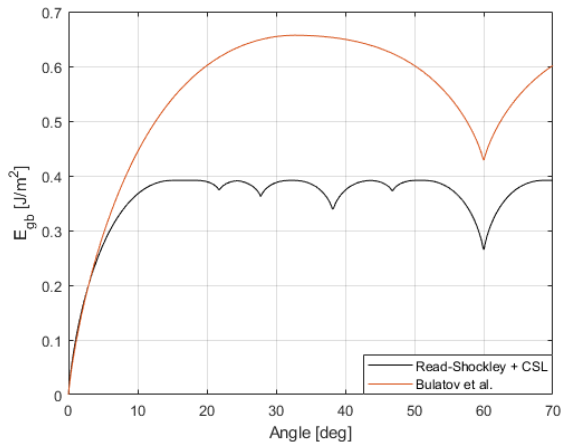


Figure 3.6: Energy as a function of the misorientation angle for a tilt around the [111] axis with the boundary in the [110] direction for two different models. Results from the CSL-modified Read-Shockley model in equation 3.13 is compared to the output from the Bulatov et al. “GB5DOF” model in [8].

3.2 Relationship between grain boundary energy and excess volume

In order to accommodate the misfit between adjacent grains, the lattice structure at the boundary must expand. This expansion, resulting in an extra volume compared to the perfect lattice, is called the excess volume and is one reason for the increased diffusivity at the grain boundary. Grain boundary energy has been related to the excess volume in multiple studies, for example in [57, 61, 60, 4], where an approximately linear relationship has been found between excess volume and grain boundary energy. However, due to the inherent problem in measuring excess volume these studies are simulation-based, mainly by means of molecular dynamics simulations.

Uesugi and Higashi [57] defined a relationship between the grain boundary energy E and the normalized boundary excess volume ΔV given by

$$E = \frac{2}{3}G\Delta V \quad (3.14)$$

where G is the shear modulus and the excess volume ΔV is normalized by the area of the super cell (simulation domain), thus having the dimension of length. Equation 3.14 was investigated by comparing multiple studies which reported a linear relation, but not necessarily quantified it. This data set contains seven different materials which are listed together with their respective shear modulus and lattice constant in table 3.1. The data is taken from Cardarelli [9]. The lattice constants are needed as some of the data is reported in units of the lattice constant and some in Ångström.

Table 3.1: Material properties [9].

Material	Cu	Ni	Al	Au	Fe	Mo	W
Shear modulus, G [GPa]	48.3	76	26.5	26	81.6	125.6	160.6
lattice constant, a [Å]	3.62	3.52	4.05	4.09	2.87	3.15	3.17

The collected data, together with equation 3.14 and two modified versions with alternative constants, are plotted in figure 3.7. The energy has been normalized by the shear modulus of the specific material, as given in table 3.1. As can be seen from figure 3.7 that the magnitudes match each other, although there is some spread in the data. Some outliers can be seen, but the data still seem to follow a linear trend. Possibly some modification can be made to equation 3.14 in order to account for this difference, but this has not been studied further in the present work.

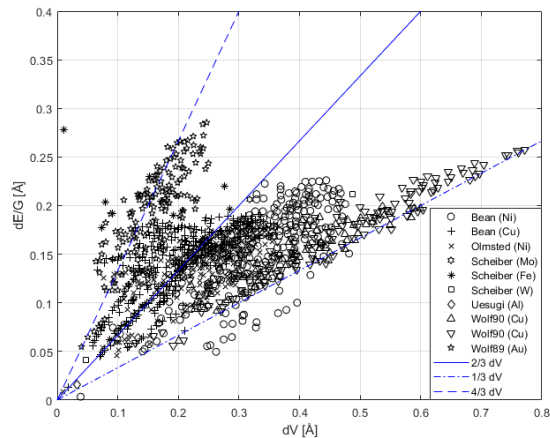


Figure 3.7: Normalized excess energy as a function of excess volume retrieved from Bean and McKenna [4], Olmsted et al. [43], Scheiber et al. [53], Uessugi and Higashi [57] and Wolf 1990 [61] and 1989 [60]. The data is compared to three linear functions.

Each data set shown in figure 3.7 was fitted using linear regression to provide the results shown in figure 3.8. It is seen that the largest deviation from equation 3.14 is found in Wolf’s calculations and the one for iron by Scheiber et al. [53]. Wolf has the earliest calculations which might make them less accurate compared to the more recent simulations. However, the author is by no means an expert in molecule dynamics and as such his comments must be seen as mere observations. In the case of iron it might be because the wrong material constants are used. The properties of iron can vary widely, depending on its crystallographic structure (the Fe “allotropes”). However, as no data was given in the report by Scheiber et al. [53], with regards to the shear modulus and the lattice constant, these were assumed according to table 3.1. It can, however, be noted that all data in the report by Scheiber et al. follow the same linear relation once the data is normalized by the lattice parameters. As can be seen in figure 3.8, Scheiber (Mo) fits the function given by equation 3.14 while the others diverge.

From this review of available data it can be said that equation 3.14 fits well enough, giving the correct order of magnitude and variation, such that it can be used as a starting point for conversion between energy and excess volume. Though interesting, further analysis of this relation is not part of the present work.

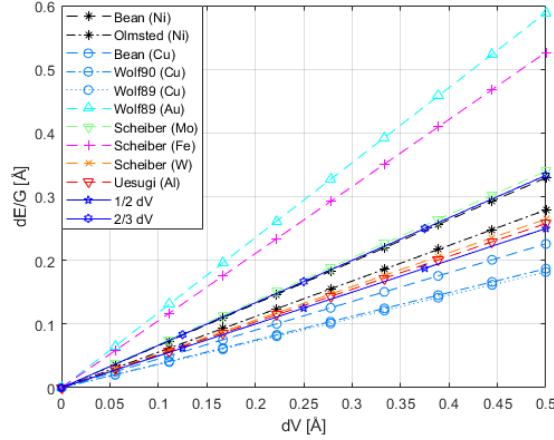


Figure 3.8: Normalized excess energy as a function of excess volume retrieved from Bean and McKenna [4], Olmsted et al. [43], Scheiber et al. [53], Uesugi and Higashi [57] and Wolf 1990 [61] and 1989 [60]. The data is compared to two linear functions.

3.3 From grain boundary energy to the diffusion coefficient

The next logical step from the previous section would be a translation between excess volume to the diffusion coefficient and thus completing the chain, allowing for translation between the grain boundary energy and the diffusion coefficient. However, a more promising and direct correlation was found between the grain boundary energy and the diffusion coefficient. This is based on the theoretical work devised by Gupta [15], in which the semi-empirical theories of Borisov et al. [5] were used, relating the diffusant mobility to the grain boundary energy. This is combined with a more recent atomic theory of diffusion, resulting in a more complete theory based on thermodynamic principles. The same methodology has been employed in multiple other studies [37, 40]. In [15] the energy is expressed by the difference in Gibbs free energy between the bulk (or volume) v and the boundary b and is found as

$$E_b = \frac{1}{2} (\Delta G_v - \Delta G_b) \quad (3.15)$$

where the half comes from the fact that the boundary is shared between two crystals. Furthermore, the diffusion coefficient is defined as

$$D = \Gamma \beta^2 f \nu \exp\left(-\frac{\Delta G}{RT}\right) \quad (3.16)$$

where Γ is a geometrical factor, β is the jump distance, f is a correlation factor, ν is the jump frequency, R the gas constant and T the absolute temperature [16]. In addition, ΔG is the Gibbs free energy, defined as $\Delta G = \Delta H - T\Delta S$ with ΔH being the enthalpy and ΔS the entropy. Following [16], and assuming that the pre-exponential term is equal for the lattice and the boundary, the energy can be written as

$$E_b = \rho RT \ln\left(\frac{D_b}{D_v}\right) \quad (3.17)$$

where ρ is a conversion factor, to provide consistent units as E_b is given in J/m^2 , defined as

$$\rho = 1/2\alpha^2 N_0 \quad (3.18)$$

where N_0 is Avogadro's number and α is the mean distance between atoms at the interface which, as suggested in [16], is set equal to the lattice constant as a first approximation. On this basis, an expression for the grain boundary diffusion can be obtained from equation 3.17 as

$$D_b = D_v \exp\left(\frac{E_b}{\rho RT}\right) \quad (3.19)$$

From equation 3.19 it can be noted that $E_b = 0$ provides $D_b = D_i$, as expected. Naturally, the lattice diffusion will also be temperature dependent, in most cases following the Arrhenius relation, equation 2.7.

To test the validity of equation 3.19, the model is compared to experimental data on diffusion of gold (Au) in copper (Cu), as measured by Budke et al. [7]. The grain boundary diffusion was measured at four different temperatures for a [100] tilt boundary and for misorientation angles around a $\Sigma = 5$ boundary.

The energy was calculated using the model by Bulatov et al. [8]. The bulk diffusion of gold in copper is taken from Divinski et al. [12], which provides

$$D_v^{Au} = 0.8 \times 10^{-5} \exp\left(-\frac{191.0 \times 10^3}{RT}\right) \quad (3.20)$$

and is given in m^2/s , and thus D_v in equation 3.19 is set to D_v^{Au} . The data from [7] is given as the triple product $s\delta D_{gb}$. The segregation factor is given as the Arrhenius relation

$$s = 0.88 \times \exp\left(-\frac{9.7 \times 10^3}{RT}\right) \quad (3.21)$$

and δ is assumed to be 0.5nm [7]. s and δ are multiplied to the estimated grain boundary diffusion coefficient. The resulting triple product, as a function of misorientation angle, are shown in figure 3.9. The model is also shown for a segregation factor $s = 1$ as a comparison, as the segregation factor might have been overestimated.

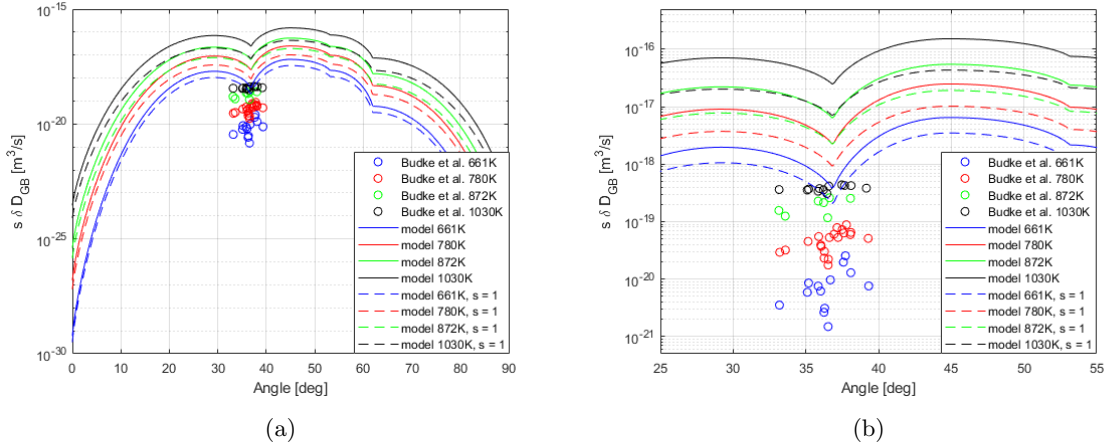


Figure 3.9: A comparison of the triple product $s\delta D_{gb}$ for gold in copper as a function of the misorientation angle for [100] symmetric tilt boundaries, as measured by Budke et al. [7], compared to that of a model. The model both use the segregation factor measured by Budke et al. [7] as well as $s = 1$. (b) is a magnification of (a).

The result in figure 3.9 seem to only be shifted in magnitude, having a relatively equal error between each temperature. It is also observed that the addition of segregation has a larger effect at high temperatures. However, the shape of the diffusion coefficient curve as reported by [7] is not captured further than in terms of the identification of the $\Sigma = 5$ dip. If this is due to limitations in the accuracy of the energy function, or if is due to errors inherent to the measurements, is still to be answered.

A modification to the α parameter, in equation 3.19, is proposed based on the fact that there is a quantifiable volume expansion at the boundary, discussed in the previous section. Firstly, as a FCC lattice can be said to be surrounded by 12 atoms, for which half are located a distance a ($=$ lattice constant) away from the center atom, and half of which are found a distance $\sqrt{2}a/2$ from the center atom, the mean distance could be considered to be the mean of these two distances, $(2 + \sqrt{2})a/4$. Secondly, the “effective” lattice parameter will be increased by the volume expansion. Following Uesugi and Higashi this expansion is found as $\Delta V = 3E/2G$ [57], as discussed in section 3.2. Based on these observations, the mean distance at the grain boundary can be expressed as

$$\alpha = \frac{(2 + \sqrt{2})(a + \Delta V)}{4} = \frac{(2 + \sqrt{2})(a + 3E/2G)}{4} \quad (3.22)$$

and as such, is a function of the material through the dependence on the shear modulus G . Using equation 3.19, and thus 3.18, together with 3.22 yields the result shown in figure 3.10. Where the used constants are given in table 3.1.

This is obviously an improvement over the previous result, provided in figure 3.9. The errors can be related to either the experiments or the model, for which the author is unsure. However, the error is smaller than the total deviation between the grain boundary diffusion and the bulk diffusion, to such an extent that it can probably be seen as negligible. Lastly, the experimental results seem to better match the modeled results using $s = 1$, which indicate that equation 3.21 might be wrong.

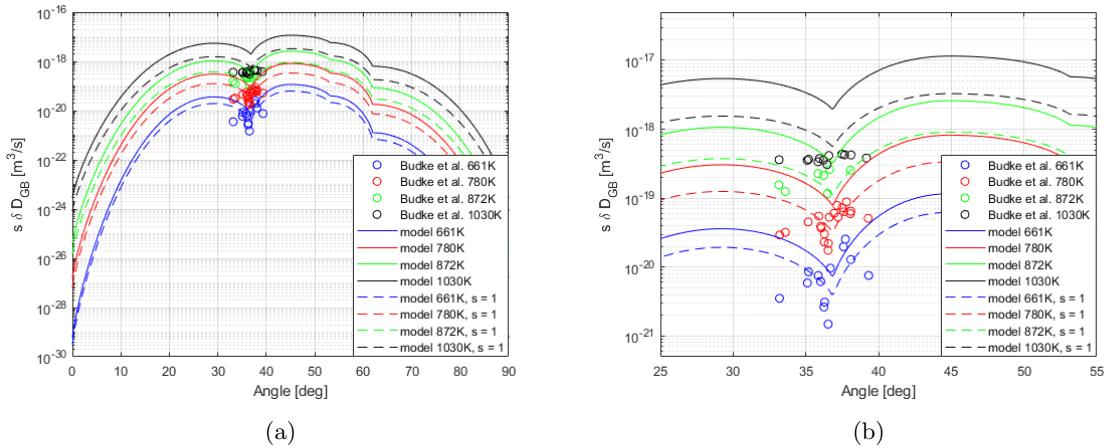


Figure 3.10: A comparison of the triple product $s\delta D_{gb}$ for gold in copper as a function of the misorientation angle for [100] symmetric tilt boundaries, as measured by Budke et al. [7], compared to that of a model. The model both use the segregation factor measured by Budke et al. [7] as well as $s = 1$. (b) is a magnification of (a).

To further give credibility to the proposed methodology, the results provided by Minkwitz et al. [37] were also studied, in which the diffusion of gold in copper is again considered, but for a [110] tilt grain boundary with the boundary plane in the [111] direction. No segregation estimation were given and therefore both $s = 1$ and equation 3.21 is used to estimate the segregation. The comparison is shown in figure 3.11. The general trend and magnitude of the model and the experimental data appear to be correlated, at least compared to the much lower bulk diffusion

It is noted, however, that as only two sets of verifying experimental data are available for the same process the proposed model cannot be considered to be fully verified. More diverse experimental data was tested but the sources often lack information such as the tilt angle and/or type of diffusing atoms. In addition, the assumed/measured value of the bulk diffusion was not found for all types of diffusing atoms, which is a necessary parameter for the suggested model. The energy model, of course, is also limited in

terms of accuracy. To more rigorously test the proposed model a dedicated experimental campaign would be appropriate, but such an investigation is beyond of the scope of this work.

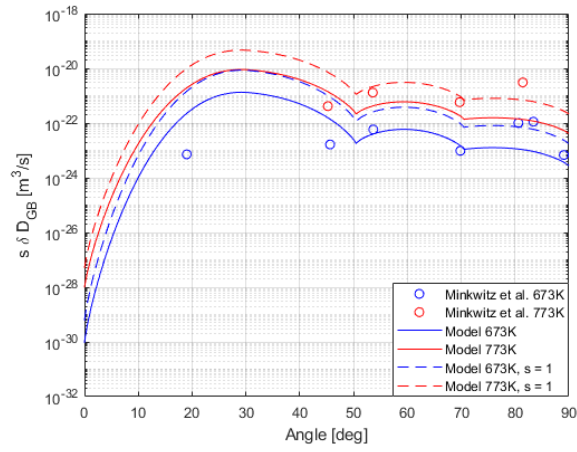


Figure 3.11: A comparison of the triple product $s\delta D_{gb}$ for gold in copper as a function of the misorientation angle for $[110]$ symmetric tilt boundaries, as measured by Minkwitz et al. [37], compared to that of a model. The model both use the segregation factor measured by Budke et al. [7] as well as $s = 1$.

Chapter 4

Computational and numerical framework

In order to implement the developed diffusion model, described in the previous chapter, a numerical method must be chosen. For this work the finite element method is used as it is a well known method and can account for quite arbitrary geometries. Furthermore, a level set description is utilized to keep track of the location of grain boundaries and the orientation of grains. Using a level set formulation will also enable further development of the model, excluded from this work, to also consider grain boundary migration by grain growth, as in Hallberg [17].

4.1 Finite element formulation

Fick's second law can be formulated in terms of the finite element (FE) method as done by Eslami [13]. The governing system of equations can compactly be written as,

$$\mathbf{C}\dot{\mathbf{a}} + \mathbf{K}\mathbf{a} = \mathbf{f} \quad (4.1)$$

where \mathbf{C} is the capacity matrix, \mathbf{K} is the stiffness matrix, \mathbf{a} is the concentration at the nodes and \mathbf{f} is the force vector. As transient diffusion is considered, a time discretization must also be made and is described later in this chapter.

A combination of MATLAB and Fortran is used to solve the problems in this study. Some of the FE-code utilize the CALFEM packages [2]. CALFEM does not, however, include a method to provide the \mathbf{C} matrix. Following [13], the element capacity matrix for a triangular element can be constructed as

$$\mathbf{C}_e = tA_e \begin{bmatrix} 1/6 & 1/12 & 1/12 \\ 1/12 & 1/6 & 1/12 \\ 1/12 & 1/12 & 1/6 \end{bmatrix} \quad (4.2)$$

where t is the thickness and A_e is the area of the element.

4.1.1 Determining the diffusion coefficient of the element using barycentric coordinates

The element diffusivity, D_e , is needed for the stiffness matrix \mathbf{K} in equation 4.1. This single value is a material property that is set constant for the whole element and must thus be chosen consciously. Because the diffusion coefficient is only known at the nodes of the element, an interpolation must be made. If there is a large difference between the diffusion coefficients at the nodes, the choice of interpolation point will make a considerable difference.

The coordinate at which the element diffusion coefficient should be taken can be described effectively by the barycentric coordinates $[\lambda_A, \lambda_B, \lambda_C]$ for which the coordinate values describe the relative position of a point P within a triangle defined by the vertices A , B and C , as illustrated in figure 4.1. a , b and c are some scalars chosen to yield the correct lengths of each side. For the barycentric coordinates it holds that $\lambda_A + \lambda_B + \lambda_C = 1$.

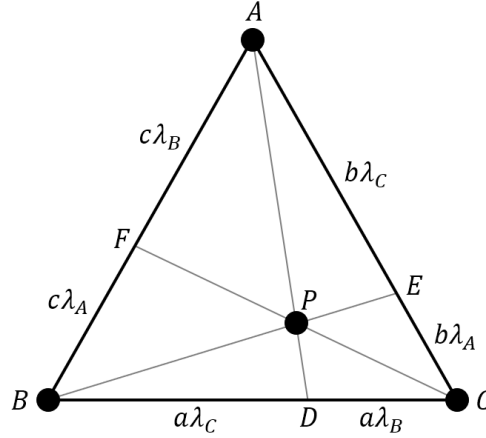


Figure 4.1: Triangle in which point P has the barycentric coordinates $[\lambda_A, \lambda_B, \lambda_C]$.

In this work the center of mass is used when evaluating the element diffusion constant D_e . The barycentric coordinates of the center of mass are easier to find by first considering the case of the fulcrum in figure 4.2, which can also be viewed according to figure 4.1 by setting the mass of point B to zero. In this cases the point masses A and B are m_A and m_B respectively.

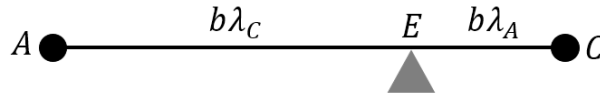


Figure 4.2: Fulcrum with two masses in each end balanced at point E .

In the case of point E in figure 4.2 being placed precisely at the center of mass, the magnitude of the moments caused by each mass will be equal, and hence

$$m_A b \lambda_C = m_C b \lambda_A \quad (4.3)$$

In this case $\lambda_B = 0$ and therefore

$$\lambda_A + \lambda_B + \lambda_C = \lambda_A + \lambda_C = 1 \Leftrightarrow \lambda_A = 1 - \lambda_C \quad (4.4)$$

Combining equation 4.3 and 4.4 yields

$$m_A b \lambda_C = m_C b (1 - \lambda_C) \Leftrightarrow \lambda_C = \frac{1}{1 + (m_A/m_C)} = \frac{m_C}{m_C + m_A} \quad (4.5)$$

Inserting the result from equation 4.5 into 4.4 yields

$$\lambda_A = 1 - \frac{m_C}{m_C + m_A} = \frac{m_A}{m_C + m_A} \quad (4.6)$$

and thus the two unknowns λ_C and λ_A have been found.

Similar expressions to those of equation 4.5 and 4.6 are found for the case of the triangle in figure 4.1, with the only difference being an added mass term in the denominator according to

$$\lambda_A = \frac{m_A}{m_A + m_B + m_C}, \quad \lambda_B = \frac{m_B}{m_A + m_B + m_C}, \quad \lambda_C = \frac{m_C}{m_A + m_B + m_C} \quad (4.7)$$

Barycentric coordinates can be transformed into Cartesian coordinates according to

$$\mathbf{r}_P = \lambda_A \mathbf{r}_A + \lambda_B \mathbf{r}_B + \lambda_C \mathbf{r}_C \quad (4.8)$$

for which \mathbf{r}_i is the Cartesian coordinate of node i .

4.1.2 Solving the first order differential equation

In order to solve the system of first order differential equations in equation 4.1, a time discretization is made using a finite difference method. A general such discretization, is provided by the theta method. Letting n and $n + 1$ denote two subsequent time steps, the theta method can be stated as

$$\mathbf{C} \frac{\mathbf{a}_{n+1} - \mathbf{a}_n}{\Delta t} + \mathbf{K}(\theta \mathbf{a}_{n+1} + (1 - \theta) \mathbf{a}_n) = \theta \mathbf{f}_{n+1} + (1 - \theta) \mathbf{f}_n \quad (4.9)$$

where Δt is the time step and $\theta \in [0, 1]$. Different time integration schemes are obtained for different choices of θ . For $\theta = 1$, the method is the implicit backward Euler method, $\theta = 0$ provides the explicit forward Euler method and with $\theta = 1/2$, the Crank-Nicolson method is retrieved [25].

Some caution must be used when choosing the time integration method, as well as the time step Δt , in order to get a stable and convergent solution. Firstly, it can be noted that an explicit method is prone to instability for larger time steps, the stability is thus conditional, whereas the implicit and Crank-Nicolson methods are unconditionally stable. For subsequent simulations in this work the implicit method is utilized. Secondly, there exists both a lower and an upper bound on the time step size in order to get physically compliant solutions. Too big time step and the error becomes too big, but conversely a too small time step can cause boundary-induced error in the first iteration because of the ‘‘shock-wave’’ initially present if the field is set to zeros or some other value that is not physically compliant with the boundary condition. Thus convergence studies must be conducted.

4.2 Level set formulation

The level set formulation, introduced by Osher and Sethian [44], is used to describe the location of interfaces. A level-set representation of a circular grain is shown in figure 4.3, where the red circle indicate the grain boundary, i.e. the zero contour of the level set. Within the grain the level set field has a positive value and outside it is negative. The magnitude of the field value at any point in the domain is the distance to the interface, thus it has a value of zero precisely on the interface. The most trivial extrapolation to a polycrystal scenario involves the addition of multiple level sets, one for each grain. This makes it trivial to know which grain an element is part of, as that level-set will be positive and the others will be negative in the element, as long as the element discretization is adapted to trace the interface contours. The level set property of being a distance function will be put to use in the modelling of the grain boundary diffusion coefficient distribution in the present work.

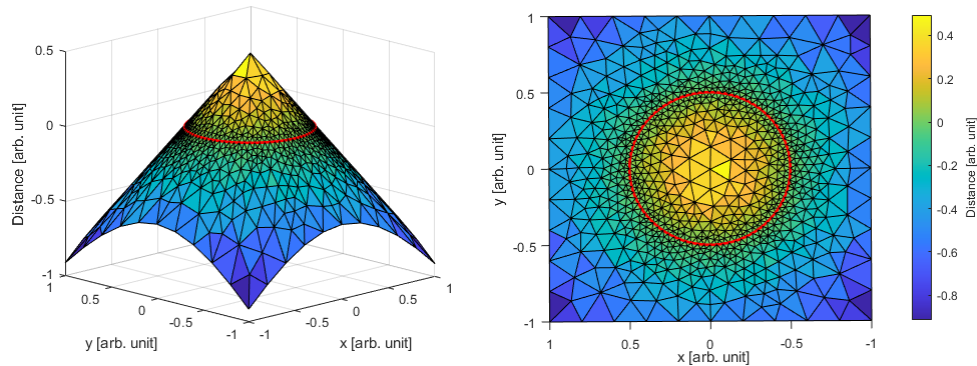


Figure 4.3: Level-set formulation of a circular grain whose boundary is marked by the red circle. The magnitude in the z-direction, as well as the colour, indicates the distance to this boundary and is positive when inside the grain and negative in the region outside of the interface.

4.3 Grain boundary diffusion coefficient distribution

This work focuses on the fact that there is generally a difference in the diffusion coefficient along the grain boundary and in the bulk (grain interior), respectively. A question then arise: How can the spatially varying diffusion coefficient be described in a numerical context? Is it a step function, as in Fisher’s model, described in chapter 2, or something smoother?

In this work the diffusion coefficient is implemented as a function of the distance to the grain boundary and incorporates structural dependencies. The diffusion coefficient is in this work modeled as an exponential function on the form

$$D(d) = D_v + (D_{GB} - D_v)e^{-\alpha d} \quad (4.10)$$

where d is the distance from the grain boundary, provided by the level set field, D_v again is the diffusion coefficient in the bulk, D_{GB} is the maximum diffusion coefficient for the grain boundary and α is a constant numerical parameter, chosen to ensure that the area beneath the exponential function

$$2 \int_0^\infty (D_{GB} - D_v)e^{-\alpha x} dx = 2 \left[(D_{GB} - D_v) \frac{1}{-\alpha} e^{-\alpha x} \right]_0^\infty = (D_{GB} - D_v) \frac{2}{\alpha} \quad (4.11)$$

has the same area as a slab (step function) with a total width of δ . Thus

$$(D_{GB} - D_v) \frac{2}{\alpha} = (D_{GB} - D_v) \delta \quad \Leftrightarrow \quad \alpha = \frac{\delta}{2} \quad (4.12)$$

This makes the model compliant with other works that model the grain boundary as a slab, as well as experimental results that assumes a certain δ .

This model will be validated in the following chapters. However, some validation can be found in the literature. Keblinski et al. [26] studied the temperature dependence of the grain boundary structure and measured the average energy per atom across a grain boundary in silicon. The resulting distribution was not a simple step function, but more or less exponential in form. The energy distribution provided in [26] is plotted in figure 4.4 together with a step function and an exponential function with the same area corresponding to that provided by equation 4.10. Because the data was calculated with plane-by-plane averages it lacks spatial resolution. Grain boundary energy is, generally, linearly dependent on the excess volume, as discussed in the previous chapter, and so the comparison is valid [57, 60, 53]. The measured energy data is linearly scaled in figure 4.4 and is found to fit the shape of the exponential function adequately.

It is recognized that this just one example, not enough to verify that this exponential distribution is a general trend. It is, however, probably not of major importance for the present mesoscopic calculations that

this grain boundary distribution function is exact, but rather that the total amount of diffused matter is correct.

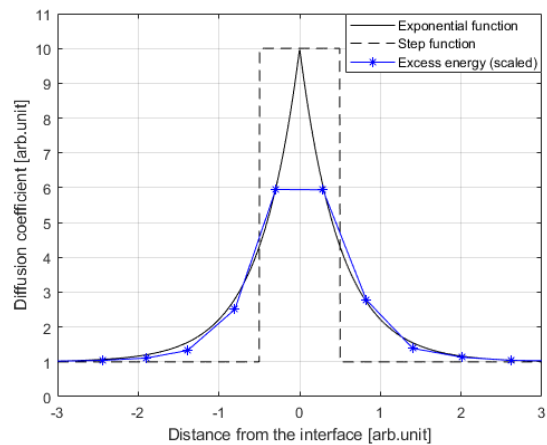


Figure 4.4: A step function and an exponential function with the same area compared to a scaled simulated energy distribution retrieved from Keglinski et al. [26].

Chapter 5

Simulation of diffusion in a bicrystal

In this chapter the simple bicrystal geometry, originally considered by Fisher [14], will be examined. The bicrystal is the simplest polycrystals possible and can be used to better control parameters, such as orientation, when taking measurements. The simple geometry also lends itself to analytical analysis methods. As there exists a plethora of reports on this very subject, both analytical and experimental, this will be the first test of the proposed model and thus a validity check of sorts. No consideration is taken regarding the structure of the grain boundary, as any misorientation dependence would yield an output correlated to the input and thus not yield anything of interest. Therefore this chapter will instead test how well the proposed grain boundary distribution model, equation 4.10, correlate with that of a slab model and how these models compare with common experimental methods for extrapolation of the grain boundary diffusion coefficient.

5.1 Model geometry and meshing

The geometry studied in this chapter is illustrated in figure 5.1. No grain boundary region is explicitly defined but is implicitly determined by considering the distance to the grain boundary interface. The concentration at nodes along the free surface is set to unity at time $t = 0$ and is held constant throughout the duration of the simulation.

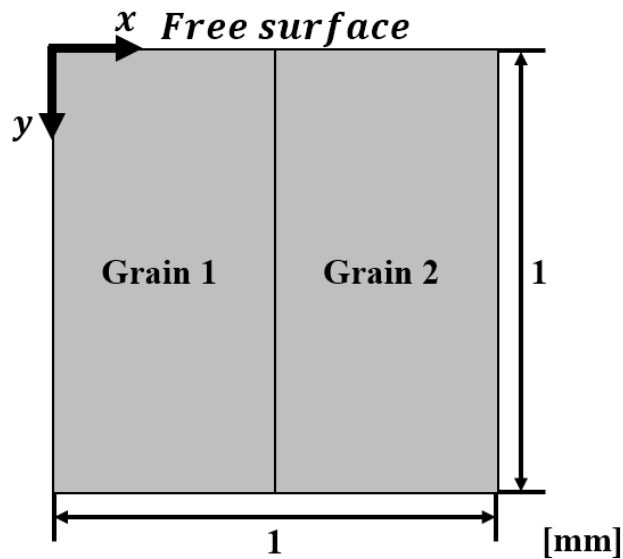


Figure 5.1: The adopted bicrystal geometry.

Six meshes were created in order to study the convergence behaviour. They are denoted by 0-5 where 0 is the coarsest mesh and an example of one of these meshes, in this case mesh 1, is provided in figure 5.2. A refined area around the grain boundary (at $x = 0.5$) is defined and an illustration of the mesh refinement parameters are shown in figure 5.3. The degree of refinement is determined according to a target segment length along the grain boundary, the thickness of one refinement element layer, as well as the number of refinement layers. The maximum element size in the rest of the domain is set to five times the target segment length. The parameters for each mesh is shown in table 5.1.

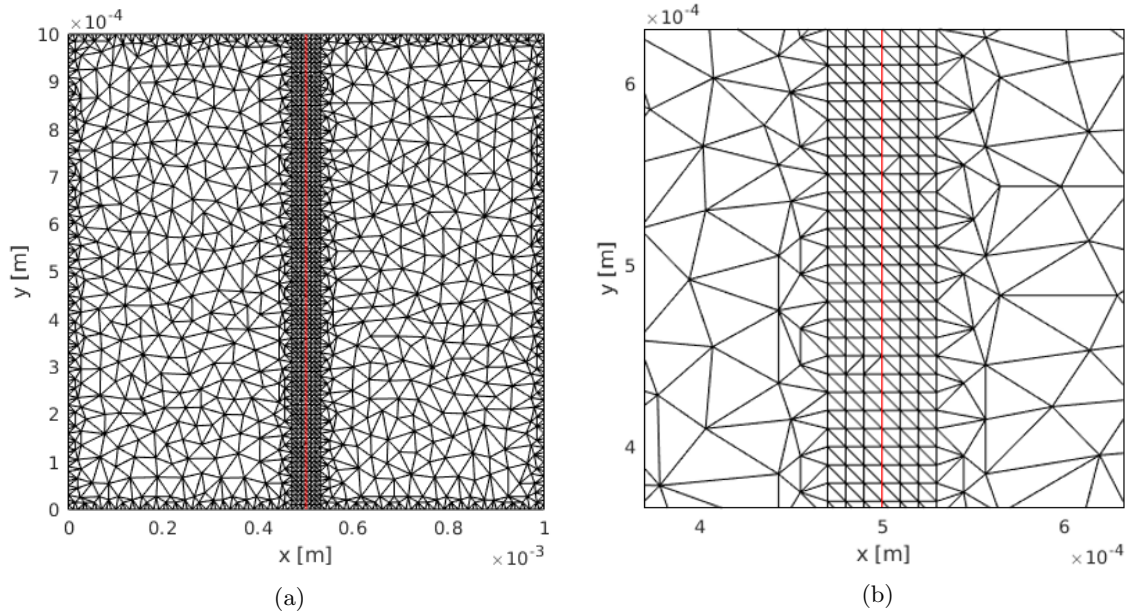


Figure 5.2: In (a) the full mesh of refinement level 1 is shown, whereas (b) is an enlargement around the grain boundary, indicated by the red line.

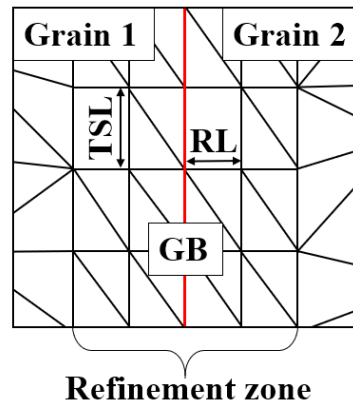


Figure 5.3: The parameters used to specify mesh refinement. GB is the grain boundary, indicated by the red line, RL the refinement layer and TSL the target segment length. In this case the mesh refinement have two refinement layers on each side of the grain boundary.

Table 5.1: Parameters defining the adopted mesh refinement levels 0-5.

Mesh number	0	1	2	3	4	5
Target segment length	0.005	0.001	0.005	0.0025	0.001	0.001
Thickness of one refinement layer	0.05	0.01	0.005	0.0025	0.001	0.0005
Number of refinement layers	2	3	6	10	17	20
Number of elements	372	3360	6113	20234	100913	107853

5.2 Convergence study using the exponential model

The convergence study is conducted using the exponential grain boundary diffusion coefficient distribution, defined in the chapter 4. In the simulations, the grain boundary diffusion coefficient is set to $D_{GB} = 10^{-7} \text{ m}^2/\text{s}$, the bulk diffusion coefficient to $D_v = 10^{-10} \text{ m}^2/\text{s}$ and the grain boundary width to $\delta = 2 \times 10^{-5} \text{ m}$. Meshes 0-4 are used together with the time steps 0.001s, 0.01s, 0.1s, 0.5s. The total concentration in the x-direction at a penetration depth of 0.3mm is plotted as a function of the time step for all the meshes in figure 5.4.

Firstly, regarding the time step, it is seen in figure 5.4 that all solutions converge to a constant value for time steps of 0.01s and below. The solutions seem to converge in a similar manner when compared to each other. Secondly, it can be seen that the results for mesh 0 and 1 are widely different from those obtained using meshes 2-4. However, from figure 5.4 it is difficult to say with certainty which level of refinement is enough for this model. Therefore a plot of the contour lines for the concentrations 0.1 and 0.8, using a time step of 0.01s, is made after 1.66s of simulation as shown in figure 5.5. It can be observed that, just as in figure 5.4, mesh 0 and 1 yield unsatisfactory results. However, zooming in around the contour lines it is seen that mesh 2 provides a somewhat uneven distribution. The same is most likely also true for mesh 3 compared to mesh 4 if the image is enlarged further, but for practical purposes mesh 3 with a time step of 0.01s is deemed good enough.

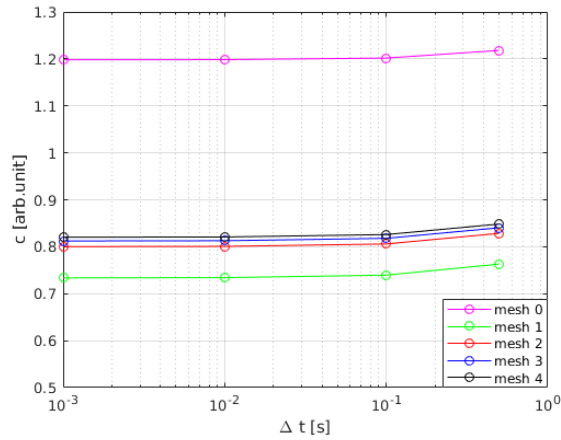


Figure 5.4: Total concentration in the x-direction at a penetration depth of 0.3mm as a function of the time step.

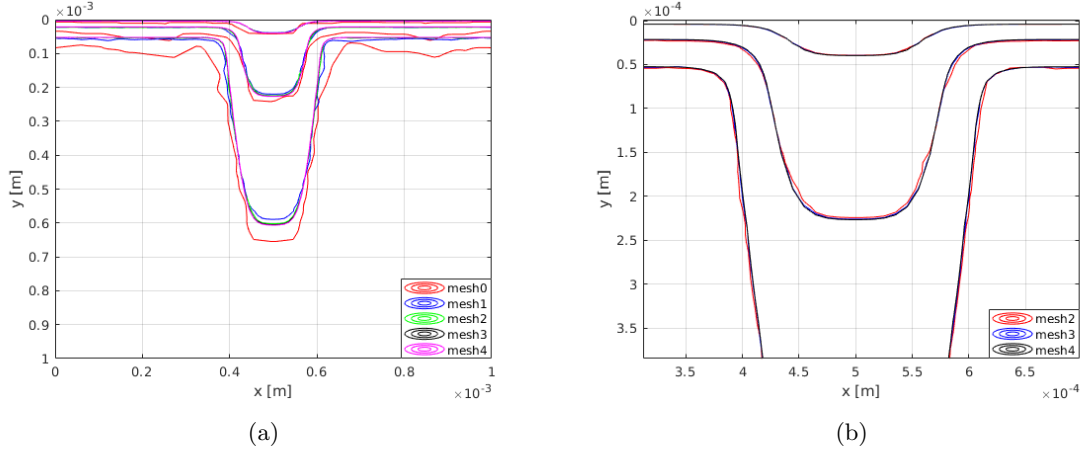


Figure 5.5: Concentration contours for the concentrations 0.1 and 0.8, using a time step of 0.01s, after 1.66s of simulation.

5.3 Comparison between Whipple’s solution and a FE-solution

In this section Whipple’s solution is compared to that obtained from a FE-simulation using the same assumptions. This means that the exponential function described in the previous chapter is replaced by a step function, defined as

$$D(d) = \begin{cases} D_{bulk} & \text{for } d > \delta/2 \\ D_{gb} & \text{for } d \leq \delta/2 \end{cases} \quad (5.1)$$

Calculations were made using the grain boundary diffusion coefficients $D_{GB} = 10^{-6}$, 10^{-7} and 10^{-8} m²/s, a bulk diffusion coefficient of $D_v = 10^{-10}$ m²/s, a grain boundary width of $\delta = 2 \times 10^{-5}$ m and a time step of 0.001s. This was done together with meshes 3-5, defined according to table 5.1. The results from the simulations, obtained after 1.66s, are shown in figure 5.6. It can be observed that the general shape of the contours are similar with the greatest deviations occurring near the grain boundary. Compared to the previous section, a noticeable difference is seen between meshes 3 and 4, and even between meshes 4 and 5. One conclusion that can be made regarding the previous section is that the exponential expression lends it self well to computer simulation stemming from its smoother spatial distribution of the diffusion coefficient compared to the step function considered in this section. What can be noted, however, on the similarity of Whipple’s solution and the FE-solution is that because of the similarity, both solution are likely correct as both arrive at the same result using widely different methodologies.

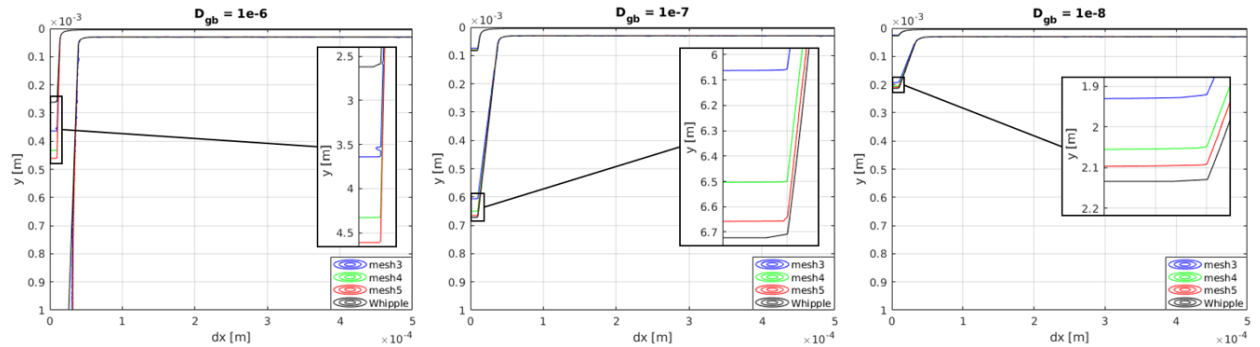


Figure 5.6: An FE-simulation compared to the analytical solution by Whipple.

5.4 Extraction of grain boundary diffusion coefficients from penetration profiles

In this section the developed model will be used to examine the validity of experimental methodologies used to measure diffusion coefficients in bicrystal systems. This has merit as all the system parameters are known and thus estimated grain boundary diffusivities extracted from penetration profiles can be examined. Type B conditions are of extra interest as a simplified version Whipple’s analytical solution was used to derive the mathematical framework used to calculate the grain boundary diffusion coefficient [32], a method that, in one form or another, is used in all experimental studies of type B measurements known to the author. By using Whipple’s solution, a slab model of the grain is assumed and might therefore result in a different penetration profile than that from a system assuming an exponential distribution. In the previous section Whipple’s solution and the FE-solution was found to be equivalent and therefore Whipple’s equation will be used for this comparison instead of a simulation.

For the simulations mesh 4, with a time step of 0.01s, was used together with the parameters in table 5.2. Mesh 4 was used as the grain boundary width δ was reduced in one case in order get the correct conditions for type B diffusion. The used parameters are listed in table 5.2. Segregation is not considered and as such $s = 1$.

Table 5.2: Parameters used in simulations of a bicrystal system for type A, B and C diffusion.

	D_{GB} [m ² /s]	D_v [m ² /s]	δ [m]	t [s]
Type A	10^{-7}	10^{-8}	10^{-5}	2
Type B	10^{-7}	10^{-10}	10^{-6}	1
Type C	10^{-7}	10^{-12}	10^{-5}	0.8

The model was first tested for a solid with the same diffusion coefficient in the whole domain, with a diffusion coefficient of 10^{-7} m²/s, the highest that is used in the simulations. The simulation was run for 2s after which a complementary error function was fitted, which is to be expected for a constant source, as discussed in chapter 2, equation 2.6. A perfect correlation was found between the extrapolated diffusion coefficient and the actual value of 10^{-7} m²/s. This means that the domain is large enough to not induce any prominent boundary effects.

In the following section the results from the three cases in table 5.2 are shown and discussed. In these sections the “true value” refer to the chosen grain boundary diffusion coefficient listed in table 5.2. A discussion of all the results is provided at the end of the chapter.

5.4.1 Type A diffusion

The resulting penetration profiles and contours for the type A diffusion case is shown in figure 5.7, for which the complementary error function, equation 2.6, have been fitted to the data, using $c_0 = 1$ as the source was set to unity. The grain boundary diffusion coefficient was extracted according to equation 2.14 using $f = \delta/10^{-3}$, where δ is the grain boundary width and 10^{-3} is the width of the domain in meters.

A good correlation between the simulation result and Whipple’s solution is found. However, the penetration profiles do not exactly follow those of the complementary error function, such as for the solid case (same diffusion coefficient in the whole domain). However, the value of D_{GB} estimated from the simulation was 91% of the true value and the estimated value of D_{GB} using Whipple’s equation was 89% of the true value.

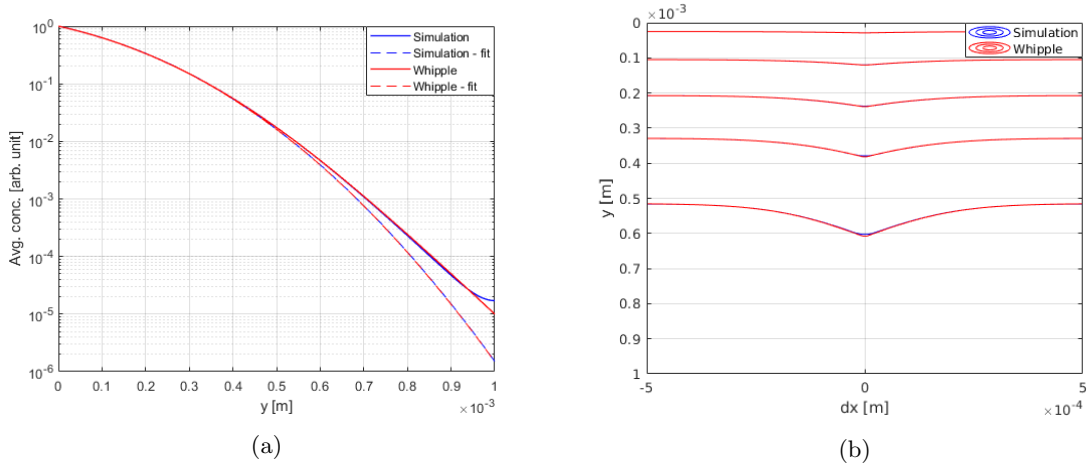


Figure 5.7: Penetration profiles (a) and contours (b) comparing the results from a simulation using an exponential distribution and Whipple’s solution (slab model) for type A diffusion. The fitted functions in (a) are complementary error functions. The contours in (b) represent the values 0.01, 0.1, 0.3, 0.6 and 0.9.

5.4.2 Type B diffusion

The resulting penetration profiles and contours for the type B diffusion case is shown in figure 5.8. The chosen values, shown in table 5.2, corresponds to Le Claire’s parameters $\beta = 250$ and $\alpha = 0.05$, defined in equation 2.16. These values are within the required interval and Le Claire’s formula, equation 2.15, can therefore be used, utilizing the slope of the tail region in figure 5.8 using the fitted lines. The estimated value of D_{GB} from the simulation was 71% of the true value and 100% of the true value for Whipple’s solution. Thus a larger difference in the result is seen between the simulation and Whipple’s solution compared to that found in the type A case. Still, the contours in figure 5.8 are similar.

The perfect correlation found when using Whipple’s solution might not be unexpected, but indicate that the variables were chosen sensibly. Furthermore, Le Claire’s equation assumes that Whipple’s equation is correct, which in turn assumes that a slab model of the grain boundary is correct, or at least satisfactory. Different assumptions, of course, often lead to different outcomes. However, this study is too small to with any certainty be able to state that this methodology, devised by Le Claire, is wrong.

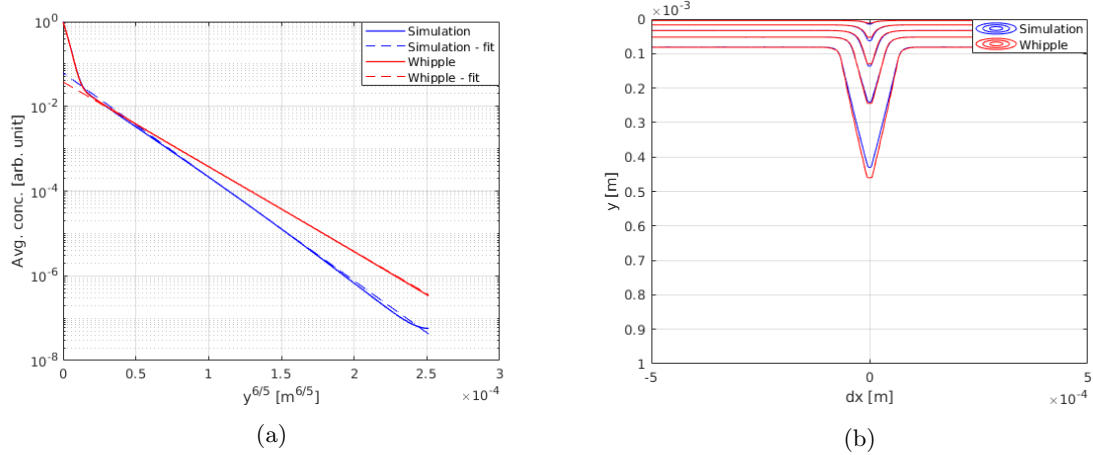


Figure 5.8: Penetration profiles (a) and contours (b) comparing the results from a simulation using an exponential distribution and Whipple’s solution (slab model) for type B diffusion. The fitted functions are lines in the semi-log plot. The contours in (b) represent the values 0.01, 0.1, 0.3, 0.6 and 0.9.

5.4.3 Type C diffusion

Finally, the resulting penetration profiles and contours for the type C diffusion cases are shown in figure 5.9. It is observed that the largest difference between the models are observed in this case, compared to the previous two cases. Furthermore, as has been shown before and is observed in figure 5.9b, the exponential relation leads to more diffusion perpendicular to the grain boundary.

As was mentioned in chapter 2, the penetration profiles should follow that of the complementary error function, equation 2.6. However, a sharp dip is observed at low penetration depths, in figure 5.9a, which is due to that diffusion only occur at the grain boundary and there is a thus a lower “effective” source at the free surface equivalent to the active area for which diffusion at the grain boundary occur. Therefore the constant c_0 in equation 2.6 should not be set to unity, but instead be fitted to the data.

In figure 5.9a it is observed that Whipple’s solution indeed follow that of a complementary error function whereas the simulation does not. However, from the fitted complementary error functions the value of D_{GB} estimated from the simulation was 14% of the true value and using Whipple’s equation it was estimated to be 87% of the true value.

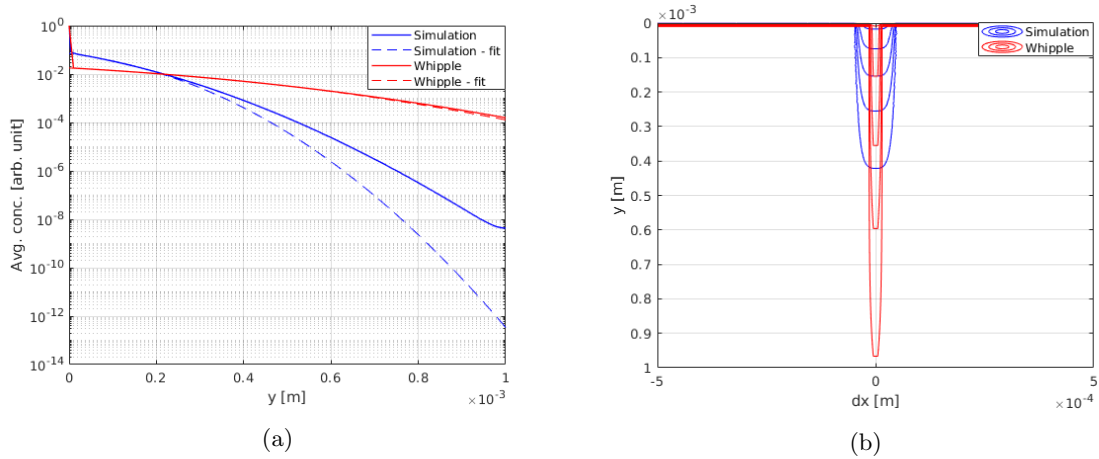


Figure 5.9: Penetration profiles (a) and contours (b) comparing the results from a simulation using an exponential distribution and Whipple’s solution (slab model) for type C diffusion. The contours in (b) represent the values 0.01, 0.1, 0.3, 0.6 and 0.9.

5.4.4 Discussion

As is evident from these three comparisons, the exponential distribution yields results that are not compliant with the methodologies used to extract the grain boundary diffusivity from experiments that use constant sources. It is found that Whipple’s solution produce better results, which is, again, not surprising as the methods themselves are based on Whipple’s solution.

However, the validity of either method can not be stated and the good correlation found between the proposed model, derived in chapter 3, and measured values can not be ignored. One difference that can be noted, however, is that the measurements that was compared to the model (figure 3.10 and 3.11) was measured using instantaneous sources (thin-film solutions). Using the same assumptions in the model might have shown better correlation with the true values using the same methods.

Chapter 6

Simulation of diffusion in a polycrystal

This chapter is dedicated to the simulations of diffusion in larger polycrystals and investigates the effect of the diffusion coefficients orientation dependence in a more realistic model system. In an even more realistic case, than the one used in this work, grain and boundary reorientation due to continuous grain boundary migration and grain growth would have to be considered, as lower boundary energy configurations might be develop during these processes. This is, however, out of scope for this work, but still something to be kept in mind for future investigations.

6.1 Model geometry and meshing

The polycrystals studied in this chapter are generated using randomly placed Voronoi seeds (grain nucleation site) aiming at an average grain size of approximately $0.2\mu\text{m}$, which is somewhat smaller than the range $2 - 162\mu\text{m}$ investigated by Noh et al. [42] in a study on copper. This choice was made to provide a larger relative grain boundary width, set to 0.5nm , such that larger elements could be used with less computational demand.

An example of a generated and meshed domain with 20 grains is shown in figure 6.1. A domain with 500 grains was also created, and will be used in the later part of this chapter. Four mesh refinements were adopted, defined by the values in table 6.1. The maximum target element size is four times that of the target segment length. The refinement layer nomenclature was explained in the previous chapter, in conjunction with figure 5.3.

The larger model have the same grain refinement and only differ in the number of grains, which means that the conclusions from the smaller, computationally less demanding, model, in terms of convergence, can be transferred to the large model.

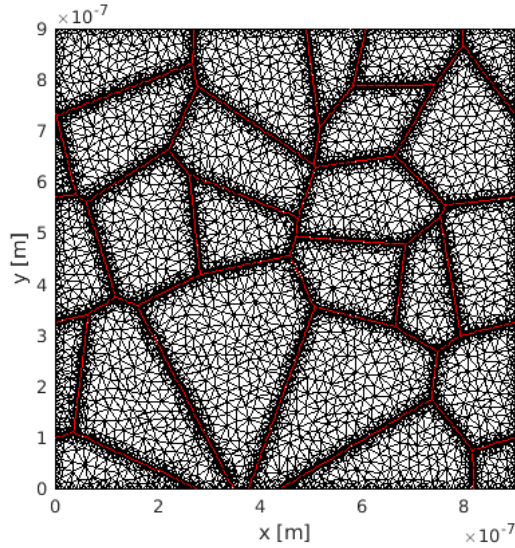


Figure 6.1: Full mesh of refinement level 1 for 20 grains. The red lines indicate the position of the grain boundaries.

Table 6.1: Parameters defining mesh refinements 0-3.

Mesh number	0	1	2	3
Target segment length (nm)	12	6	1.5	1.5
Thickness of one refinement layer (nm)	6	3	3	0.75
Number of refinement layers	1	2	4	8

6.2 Convergence study

It was realized that the convergence study in the last chapter is less applicable to the polycrystal models as it suggests a much too fine grid, which would result in excessive computation times. A new convergence study was made, using the four meshes defined in table 6.1 and four different time steps. The 20-grained domain in figure 6.1 was used together with the model described in chapter 3 at a temperature of 900K.

The calculations were compared in terms of the average concentration in the domain, measured at 1,000,000 evenly spaced points. Both the total concentration and the concentration as a function of penetration depth was considered and the results are shown in figure 6.2. It is seen that the solution converges for the considered time steps but not for the mesh refinement. However, in order to have reasonable simulation times mesh 2 is used as the penetration profile is similar to that obtained when using mesh 3. The increased diffusion in mesh 2 might be due to the weighting of the element diffusion coefficient and thus this increased (error) will be the same for all simulations. As long as simulations are compared directly with each other, this will not affect the conclusions.

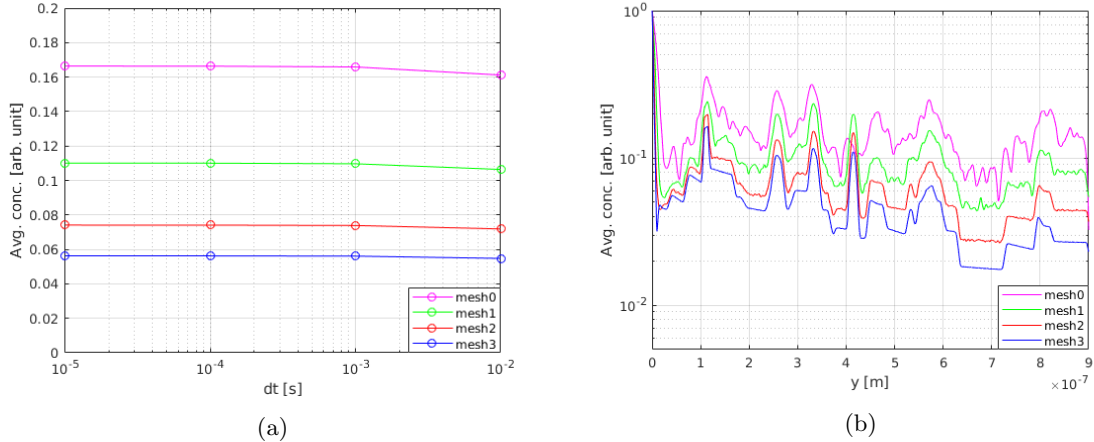


Figure 6.2: Average concentration in the domain as a function of the time step (a) and the average concentration as a function of penetration depth (b) for the four mesh refinements.

6.3 Comparison with experiments

Comparing simulations and experiments is usually difficult as all necessary parameters must be available. In the cases of comparing experimental data on polycrystals, the crystallographic texture must be known. This texture is in part due to that during pre-processing of specimens, and during the initial crystallization, the crystal structure will evolve to orientations that minimize the energy of the system and will therefore not necessarily be described by a Mackenzie distribution. This concerns not only to the individual grain orientations, but also to the local grain boundary character, as noted in [48].

Experimental diffusion measurements are often conducted in the Harrison type C regime for which the effective grain boundary diffusion can be measured directly [47, 11]. This implies that it can not, at least not with common measurement techniques, measure the orientation dependant diffusion coefficient, as provided by bicrystal experiments, but rather an “effective”, or mean, diffusion coefficient. Therefore, the measured effective grain boundary diffusion will be used in a polycrystal model with constant diffusion coefficient and will be compared to models with the developed orientation dependant diffusion coefficient. The idea is that the effective diffusion would be the same, or at least similar, if the model holds any validity. Furthermore, the lack of data on the crystallographic texture in the experiment samples makes a direct comparison of the results questionable.

In Divinski et al. [11], the diffusion of silver in copper was examined and the data in [11] is used as the basis for the present comparison. In [11] the bulk diffusion is provided as

$$D_v^{Ag} = 6.1 \times 10^{-5} \exp\left(-\frac{194.4 \times 10^3}{RT}\right) \quad (6.1)$$

The grain boundary diffusion is given by

$$D_{GB}^{Ag} = 1.73 \times 10^{-4} \exp\left(-\frac{108.8 \times 10^3}{RT}\right) \quad (6.2)$$

A simulation model with 500 grains was used using mesh refinement 2 with a time step of 10⁻⁴s. Again, the grain size of the structure is smaller than typical grains, and also smaller than in the sample used in [11]. But as the results are not compared directly to the experimental data it should not make a difference. The simulation was run for 9 × 10⁻²s at 900K. This is a higher temperature than the 473 – 537K considered in [11]. However, the Arrhenius expression in equation 6.2 should still be valid for higher temperatures.

Seven simulation cases were considered, listed in table 6.2: Two random textures were used, for which case 2 only considers the relative orientation of the grains and not the inclination of the boundary plane as for case 1. For case 3 the maximum grain boundary diffusion coefficient is set according to equation 6.2. Furthermore two distinct orientations are investigated in case 4-7. In cases 5 and 7 some angular spread is added to the orientations, where the angular spread is some random scatter defined by a Gaussian with a width defined by the spread. The two specific orientations in case 4-7 is listed in table 6.3. The impact of the grain boundary normal was also investigated for orientation 1 in case 7.

Table 6.2: Texture cases for the polycrystal model.

Case 1	Random
Case 2	Random, not considering n_{GB}
Case 3	Fixed
Case 4	Orientation 1 with 0° spread
Case 5	Orientation 1 with 20° spread
Case 6	Orientation 2 with 0° spread
Case 7	Orientation 1 with 20° spread, not considering n_{GB}

Table 6.3: Orientations used for cases 4-7. Orientation 1 represents a so called “rolling” texture [30].

Name	Euler angles [deg]
Orientation 1	[90, 35, 45]
Orientation 2	[39, 66, 27]

The angular spread around the ideal texture is applied to orientation 1, in cases 5 and 7, which results in a distribution of misorientation angles. This distribution and the boundary types are illustrated in figure 6.3. Of course, a maximum spread larger than 20° is possible as it is defined by a Gaussian that tails off to a certain degree. Because the maximum misorientation angle is larger than the Brandon criteria used (15°), not all boundaries are $\Sigma = 1$ boundaries.

In the case of the random boundaries, seen in figure 6.4, the misorientations show a good correlation to the Mackenzie distribution, discussed in chapter 2, which indicate that the model is large enough to have a good statistical behavior. In figure 6.4b it is seen that also the random texture have some $\Sigma = 3$ twin boundaries. If relaxation, by means of grain boundary migration and grain growth, were to be considered the distribution of Σ values might be different.

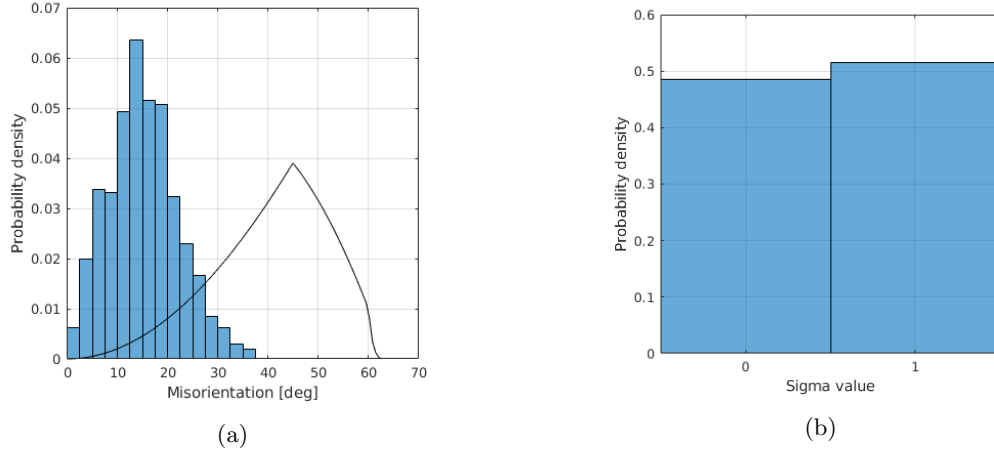


Figure 6.3: In (a) the distribution of misorientation angles for a textured polycrystal is shown, where the black line represent the Mackenzie distribution for a truly random texture. In (b) the corresponding sigma values are shown and characterized by the Brandon criteria.

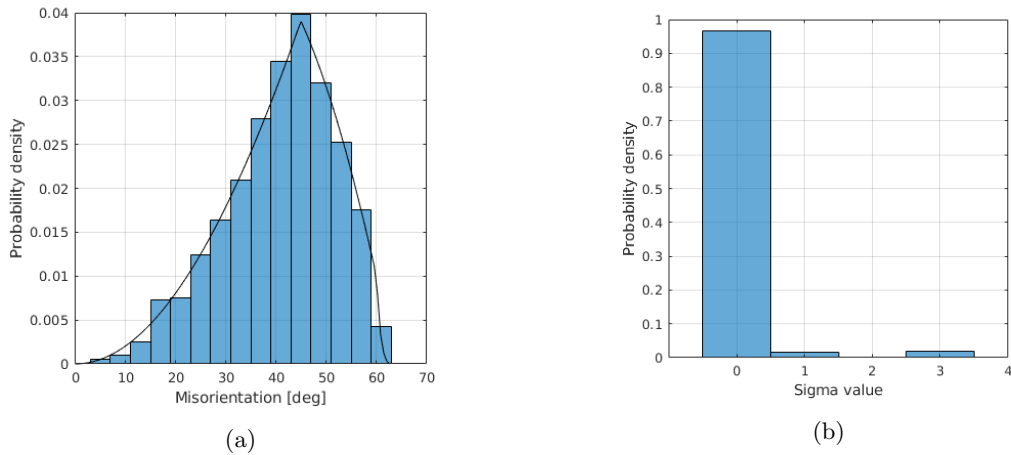


Figure 6.4: In (a) the distribution of misorientation angles for a randomly texture polycrystal is shown, where the black line represent the Mackenzie distribution for a truly random texture. In (b) the corresponding sigma values are shown and characterized by the Brandon criteria.

The resulting penetration profiles are shown in figures 6.5 and 6.6. One case was omitted in figure 6.5 for clarity. It is seen that there is good correlation between case 3 and case 4, a somewhat better correlation is found with case 5. The increased diffusivity of orientation 1 might be circumvented if reorientation would have been considered. Since the texture was not given in [11] it is not known if their sample preparation included rolling as part of the cold deformation, that is indeed mentioned, though it is a possibility and would help to explain the results. As for now, these are just speculations.

A comparatively significant difference between case 3 and cases 1, 2 and 6 is observed which show the importance of orientation dependence of the effective diffusion. Furthermore, looking at the impact of also considering the grain boundary normal, which is investigated in cases 2 and 7, both of which are shown in figure 6.6, it is seen to have a larger effect on orientation 1. It might be good to point out that the grain boundary normal can not be discarded for cases with zero spread, as such a texture results in zero

misorientation, since all grains are identically oriented. As the orientations are closer to each other for case 7 compared to case 2, a lower diffusivity is expected, and indeed observed.

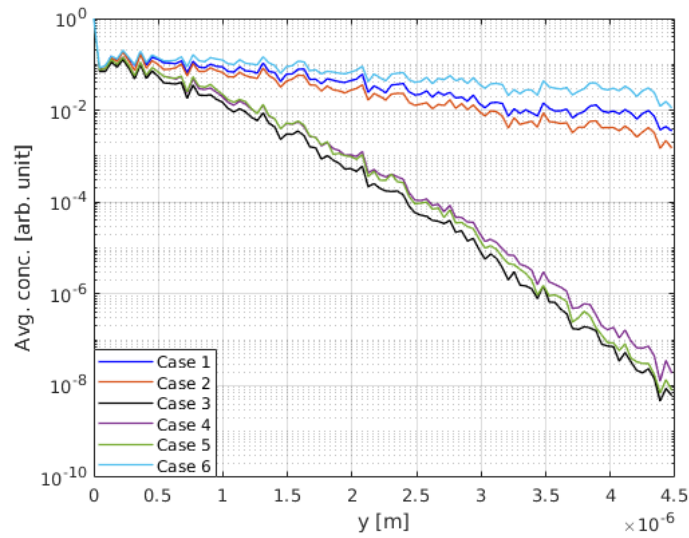


Figure 6.5: Penetration profile of six different textures, defined in table 6.2.

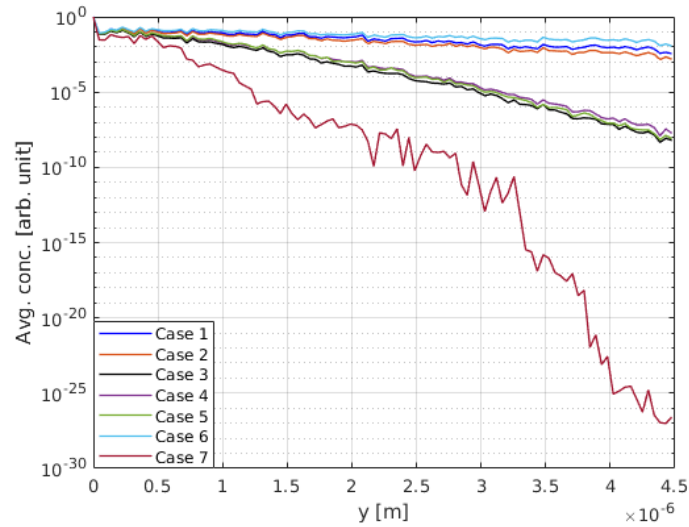


Figure 6.6: Penetration profile of seven different textures, defined in table 6.2.

Again, this comparison is by no means complete and though a good correlation is found for the chosen methodology it could be a coincidence and an accompanying experimental study with a full texture and structure characterization is need for a thorough comparison between the model and experimental data.

The concentration field obtained from the simulations using case 1 is shown in figure 6.7. No anisotropy is seen in the field with regards to the individual boundary paths. It can be noted that for all intents and purposes the system can be said to be in the type C kinetic regime.

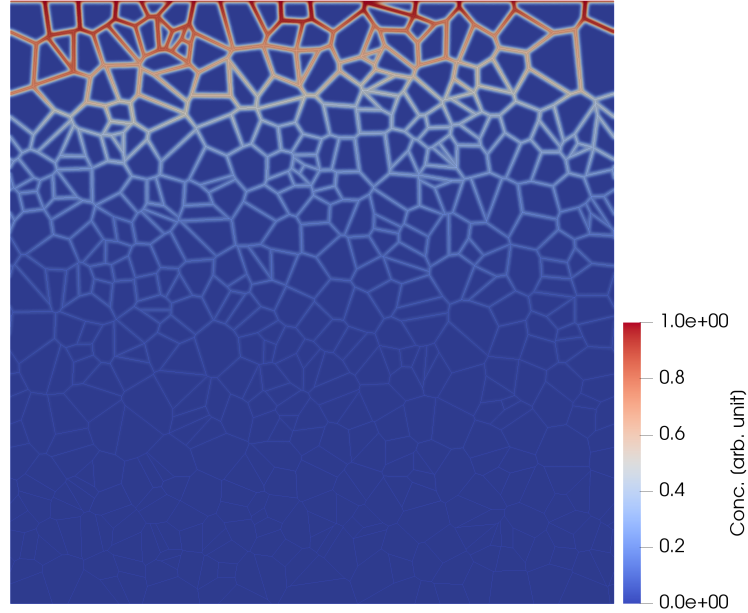


Figure 6.7: Concentration field for a polycrystal with a random texture.

6.4 Extraction of grain boundary diffusion coefficients from penetration profiles

In this section the 500 grained polycrystal model will be used to examine the validity of experimental methodologies used to measure diffusion coefficients in polycrystal systems, as was done on bicrystals in chapter 5. Orientation dependence is, however, not considered in order to better control the active kinetic regime, as the grain boundary diffusion would vary. As Whipple's solution is of no use in this comparison a slab model for the grain boundary is utilised instead, together with the exponential model. The used parameters are listed in table 6.4 and the methods that are used are the same as in chapter 5 and are discussed in the following sections.

Table 6.4: Parameters used in simulations of a polycrystal system for type A, B and C diffusion.

	D_{GB} [m ² /s]	D_v [m ² /s]	δ [nm]	t [s]
Type A	10^{-7}	10^{-8}	0.5	5e-05
Type B	10^{-6}	10^{-11}	0.5	2e-4
Type C	10^{-7}	10^{-15}	0.5	1e-4

6.4.1 Type A diffusion

The resulting penetration profile, the fitted complementary error function and the concentration field for the exponential model in the case of type A diffusion are shown in figure 6.8. As the exponential and the slab models result in the same penetration profile, only the exponential function is shown in figure 6.8a.

For the chosen variables $\sqrt{D_v t} = 2.2 \times 10^{-6}$ m which is considerably larger than the approximate grain size of 0.2 μ m, which indicate that it is indeed type A diffusion. This is also consistent with figure 6.8b, where an even concentration distribution, without any prominent grain boundary diffusion, is observed.

Furthermore, a good correlation is found between both simulations and the fitted function in terms of the shape of the penetration profile, though there seems to be some boundary effect. From the fitted

complementary error functions a perfect estimation is found for D_{GB} in both cases.

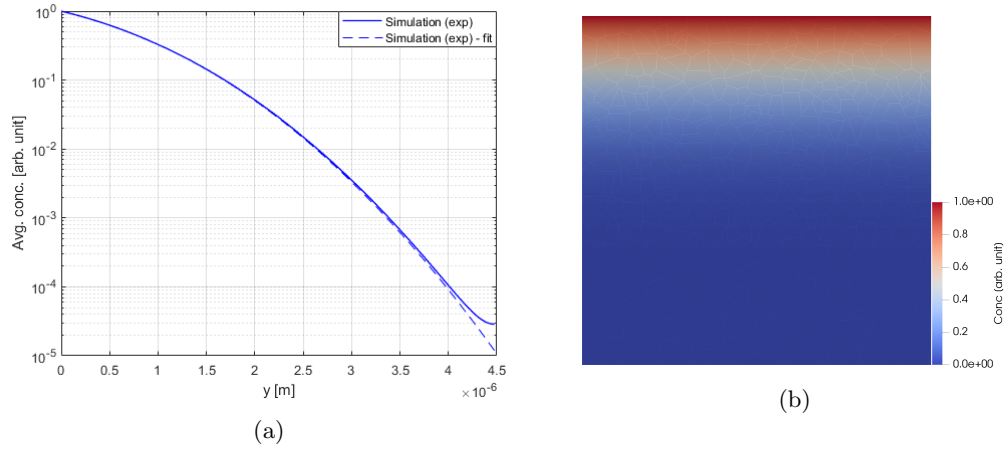


Figure 6.8: Penetration profiles (a) and concentration field (b) for the exponential model. The fitted function in (a) is a complementary error function.

6.4.2 Type B diffusion

The resulting penetration profiles, fitted functions and the concentration field for the exponential model in the case of type B diffusion are shown in figure 6.9. The chosen values, shown in table 6.4, corresponds to Le Claire's parameters $\beta = 559$ and $\alpha = 0.006$, defined in equation 2.16. These values are within the required interval for the use of Le Claire's formula, equation 2.15. From figure 6.9b it can be observed that most of the diffusion occurs along grain boundaries, with some diffusion inside the grains, consistent with type B diffusion.

Utilizing the slope of the tail region in figure 6.9a using the fitted lines, the estimated value of D_{GB} can be calculated using Le Claire's formula, equation 2.15. Equation 2.15 provides that from the simulation using the exponential function D_{GB} was 43% of the true value and using the slab model D_{GB} was 44% of the true value. In this case, unlike for the bicrystal case, the estimated values for the grain boundary diffusion coefficient are similar, but ultimately wrong.

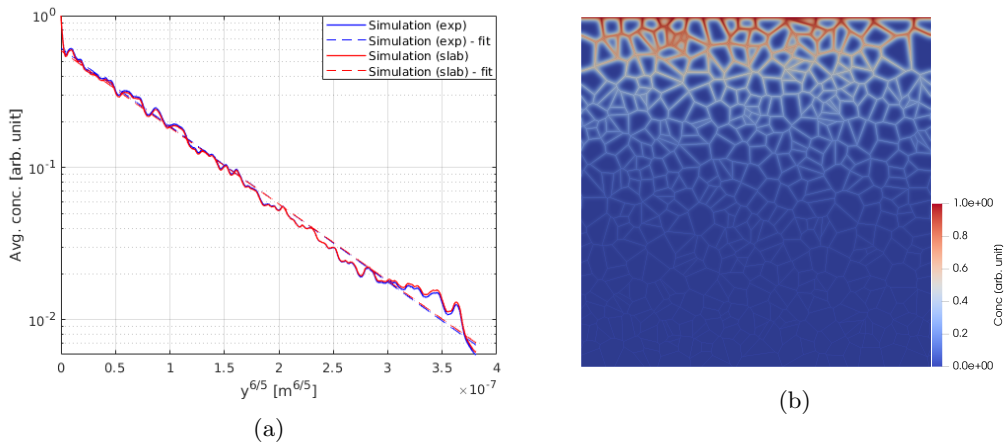


Figure 6.9: Penetration profiles (a) and concentration field for the exponential model (b). The fitted functions are lines in the semi-log plot

6.4.3 Type C diffusion

Finally, the resulting penetration profiles, fitted functions and the concentration field for the exponential model for the case of type C diffusion are shown in figure 6.10. From figure 6.10b it is evident that all diffusion effectively occur along grain boundaries, consistent with type C diffusion.

From the fitted complementary error functions, using the same method as for the bicrystal case, using an “effective” source term, the grain boundary diffusion, D_{GB} , is estimated to be 5% of the true value for the exponential function and 13% of the true value for the slab model. It can be seen that the relationship between the two models is similar to that for the bicrystal, with the exponential function yielding lower values than for a slab model. However, unlike for the bicrystal, both penetration profiles follow that of the complementary error functions. But even so, the estimations are worse than that for the bicrystal, that was estimated to be 14% and 87% of the true value.

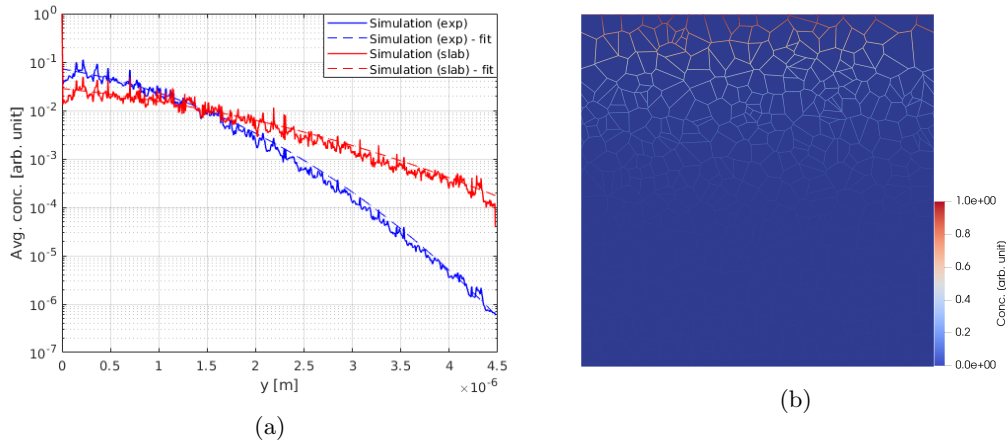


Figure 6.10: Penetration profiles (a) and concentration field for the exponential model (b). The fitted functions in (a) are complementary error functions.

6.4.4 Discussion

From these investigations it is evident that two of the common methodologies do not yield the correct results, while for type A a perfect correlation is found. Furthermore, the errors for type B and C are higher for the polycrystal cases than those for the bicrystal, the exponential and the slab model show similar errors in the polycrystal case. Again, these results are non-conclusive and more comparisons would be needed to make any statement of the validity of the methods.

Chapter 7

Summary, conclusions and closing remarks

In this report a diffusion model that consider the local grain boundary character is developed and employed in numerical simulations. The computer model is compared to multiple experimental results both in terms of the misorientation and by simulation using two different 2D geometries. Furthermore, the experimental methods frequently used to measure the grain boundary diffusion coefficient for constant sources is investigated.

7.1 Grain orientation dependent diffusion

From the comparison with experimental data, found in chapter 3, the model appears to capture the general trends and the salient features of microstructure-sensitive diffusion. The extent to which the same can be said for the polycrystal case is, however, limited, since the necessary structure and texture analysis is lacking from the experimental studies.

If the proposed model can be further verified to be an accurate model of the grain boundary diffusion it would be a major breakthrough, as only the bulk diffusion is required to be measured, which with certainty can be extracted from penetration data, at least for Fickian diffusion. Furthermore, if the volume diffusion coefficient could be retrieved from material data, by using the jump frequency etc., measurements would not be needed at all and the model would start to become more of a bottom-up model.

7.2 Measurements of the diffusion coefficient

Considering the experimental comparisons, the results were found to be unsatisfactory, especially when using an exponential grain boundary diffusion distribution. However, the data set is too small to make any suggestions on modifications to the employed methodologies. There could be some linear relationship between the estimated values and the true value not uncovered by the minimal study presented in this paper. If that is the case already measured quantities, using these methods, could be corrected.

However, what can be said from the results is that it looks like it would be beneficial to measure in the type A diffusion regime, at least when considering constant sources. It could be the case, however, that improved results are obtained if an instantaneous source is considered instead.

7.3 What the future holds

One could conceptualize a computer code that combines grain growth, as done by Hallberg [17], with the diffusion model derived in this work. This would permit simulation of (almost) the whole process in order to find which heat treatment is needed to yield the desired grain boundary diffusion, something that is of

interest to the grain boundary engineering community. This might be combined with the mechanics of cold work, and other diffusion mechanisms such as, for example, segregation to truly capture the physics of the polycrystal under various thermo-mechanical processing routes. Another attractive prospect is if the inverse problem could be solved so that when given a target diffusion coefficient, the necessary materials processing could be prescribed.

If this inversed problem was combined with other target functions, such as mechanical rigidity or hardness of the material, which are two additional examples of grain structure dependant quantities, it would begin to resemble an optimization problem. However, these aspects are just pipe dreams for now, with the basics still being figured out.

Bibliography

- [1] AKIS, R., BRINKMAN, D., SANKIN, I., FANG, T., GUO, D., VASILESKA, D., AND RINGHOFER, C. Extracting Cu diffusion parameters in polycrystalline CdTe. In *2014 IEEE 40th Photovoltaic Specialist Conference (PVSC)* (2014), pp. 3276 – 3281.
- [2] AUSTRELL, P. E., DAHLBLOM, O., LINDEMANN, J., OLSSON, A., OLSSON, K., PERSSON, K., PETERSSON, H., RISTINMAA, M., SANDEBERG, G., AND WERNBERG, P. A. *CALFEM*. Lund, 2004.
- [3] BALANDIN, I. L., AND BOKSHEIN, B. S. Temperature and orientation dependences of the grain-boundary diffusion coefficient of antimony in copper bicrystals. *Physics of the Solid State* 39, 7 (1997), 1019–1023.
- [4] BEAN, J. J., AND MCKENNA, K. P. Origin of differences in the excess volume of copper and nickel grain boundaries. *Acta Materialia* 110 (2016), 246 – 257.
- [5] BORISOV, V. T., GOLIKOV, V. M., AND SCHERBEDINSKIY, G. V. Relation between diffusion coefficients and grain boundary energy. *The physics of metals and metallography* 17, 6 (1964), 80–85.
- [6] BRANDON, D. G. The structure of high-angle grain boundaries. *Acta Metallurgica* 14, 11 (1966), 1479 – 1484.
- [7] BUDKE, E., SURHOLT, T., PROKOFJEV, S. I., SHVINDLERMAN, L. S., AND HERZIG, C. Tracer diffusion of Au and Cu in a series of near $\Sigma=5$ (310)[001] symmetrical Cu tilt grain boundaries. *Acta Materialia* 47, 2 (1999), 385–395.
- [8] BULATOV, V. V., REED, B. W., AND KUMAR, M. Grain boundary energy function for fcc metals. *Acta Materialia* 65 (2014), 161 – 175.
- [9] CARDARELLI, F. *Materials Handbook*, second ed. Springer-Verlag London, 2008.
- [10] CRANK, J. *The mathematics of diffusion*, vol. 2. Oxford University Press, 1975.
- [11] DIVINSKI, S., LOHMANN, L., AND HERZIG, C. Grain boundary diffusion and linear and non-linear segregation of Ag in Cu. *Interface Science* 11, 1 (2003), 21–31.
- [12] DIVINSKI, S. V., LOHMANN, M., SURHOLT, T., AND HERZIG, C. Grain boundary motion during Ag and Cu grain boundary diffusion in Cu polycrystals. *Interface Science* 9, 3-4 (2001), 357–363.
- [13] ESLAMI, M. R. *Finite Elements Methods in Mechanics*, vol. 216. 2014.
- [14] FISHER, J. C. Calculation of diffusion penetration curves for surface and grain boundary diffusion. *Journal of Applied Physics* 22, 1 (1951).
- [15] GUPTA, D. Influence of solute segregation on grain-boundary energy and self-diffusion. *Metallurgical transactions. Part A: Physical Metallurgy Materials Science* 8, 9 (1977), 1431–1438.
- [16] GUPTA, D. Diffusion, solute segregations and interfacial energies in some material: An overview. *Interface Science* 11, 1 (2003), 1573–2746.

- [17] HALLBERG, H. Influence of anisotropic grain boundary properties on the evolution of grain boundary character distribution during grain growth - a 2D level set study. *Modelling and Simulation in Materials Science and Engineering* 22, 8 (2014).
- [18] HALLBERG, H., AND BULATOV, V. V. Modeling of grain growth under fully anisotropic grain boundary energy. *Modelling and Simulation in Materials Science and Engineering* 27, 4 (apr 2019).
- [19] HAO, Y., TAN, C., YU, X., CHEN, R., NIE, Z., REN, Y., YANG, S., LI, Y., AND WANG, F. Effect of grain boundary misorientation angle on diffusion behavior in molybdenum-tungsten systems. *Journal of Alloys and Compounds* 819 (2020).
- [20] HARRISON, L. G. Influence of dislocations on diffusion kinetics in solids with particular reference to the alkali halides. *Transactions of the Faraday Society* 57 (1961), 1191–1199.
- [21] HASSOLD, G. N., HOLM, E. A., AND MIODOWNIK, M. A. Accumulation of coincidence site lattice boundaries during grain growth. *Materials Science Technology* 19, 6 (2003), 683 – 687.
- [22] HEITJANS, P., KÄRGER, J., HERZIG, C., AND MISHIN, Y. *Grain Boundary Diffusion in Metals*. 2005, p. 337.
- [23] HERZIG, C., AND MISHIN, Y. *Grain Boundary Diffusion in Metals*. Springer Berlin Heidelberg, Berlin, Heidelberg, 2005, pp. 337–366.
- [24] HUMPHREYS, F. J., AND HATHERLY, M. *Recrystallization and Related Annealing Phenomena*, vol. 2. Elsevier, 2004.
- [25] ISERLES, A. *A First course in the Numerical Analysis of Differential Equation*, vol. 2. 2009.
- [26] KEBLINSKI, P., PHILLPOT, S. R., WOLF, D., AND GLEITER, H. Thermodynamic criterion for the stability of amorphous intergranular films in covalent materials. *Physical review letters* 77, 14 (1996), 2965 – 2968.
- [27] KING, A. H., AND SHEKHAR, S. What does it mean to be special? the significance and application of the brandon criterion. *Journal of Materials Science* 41, 23 (2006), 7675 – 7682.
- [28] KITAGAWA, Y., IKEUCHI, K., KURODA, T., MATSUSHITA, Y., SUENAGA, K., HIDAKA, T., AND TAKAUCHI, H. Hydrogen embrittlement susceptibility of microstructures formed in multipass weld metal for HT780 class steel. *Journal of Materials Science* 43, 1 (2008), 12 – 22.
- [29] KLUGKIST, P., ALESHIN, A. N., LOJKOWSKI, W., SHVINDLERMAN, L., GUST, W., AND MITTEMEIJER, E. J. Diffusion of Zn along tilt grain boundaries in Al: pressure and orientation dependence. *Acta Materialia* 49, 15 (2001), 2941 – 2949.
- [30] KOCKS, U. F., TOMÉ, C. N., AND WENK, H. R. *Texture And Anisotropy*. Cambridge university press, 1998.
- [31] LACAILLE, V., MOREL, C., FEULVARCH, E., KERMOUCHE, G., AND BERGHEAU, J. M. Finite element analysis of the grain size effect on diffusion in polycrystalline materials. *Computational Materials Science* 95 (2014), 187 – 191.
- [32] LE CLAIRE, A. D. The analysis of grain boundary diffusion measurements. *British Journal of Applied Physics* 14, 6 (1963), 351–356.
- [33] LEVINE, H. S., AND MACCALLUM, C. J. Grain boundary and lattice diffusion in polycrystalline bodies. *Journal of Applied Physics* 31, 3 (1960), 595–599.
- [34] LIENIG, J., AND THIELE, M. *Fundamentals of Electromigration-Aware Integrated Circuit Design*. Springer International Publishing, 2018.

- [35] MACKENZIE, J. K. Second paper on statistics associated with the random disorientation of cubes. *Biometrika* 45 (1958), 229–240.
- [36] MEHRER, H. *Diffusion in Solids. Fundamentals, Methods, Materials, Diffusion-Controlled Processes*. Springer Series in Solid-State Sciences: 155. Springer-Verlag GmbH., 2007.
- [37] MINKWITZ, C., HERZIG, C., RABKIN, E., AND GUST, W. The inclination dependence of gold tracer diffusion along a $\Sigma 3$ twin grain boundary in copper. *Acta Materialia* 47, 4 (1999), 1231 – 1239.
- [38] MISHIN, Y., HERZIG, C., BERNARDINI, J., AND GUST, W. Grain boundary diffusion: fundamentals to recent developments. *International Materials Reviews* 42, 4 (1997), 155.
- [39] MISHIN, Y. M., AND RAZUMOVSKII, I. M. Analysis of an asymmetrical model for boundary diffusion. *Acta Metallurgica Et Materialia* 40, 3 (1992), 597 – 606.
- [40] MOGHADAM, M. M., RICKMAN, J. M., HARMER, M. P., AND CHAN, H. M. Orientational anisotropy and interfacial transport in polycrystals. *Surface Science* 646, Surface science for heterogeneous catalysis, a special issue in Honour of Richard Lambert (2016), 204 – 209.
- [41] MURAKAMI, Y. 21 - hydrogen embrittlement. In *Metal Fatigue (Second Edition)*, Y. Murakami, Ed., second edition ed. Academic Press, 2019, pp. 567 – 607.
- [42] NOH, H. J., KIM, J. W., LEE, S. M., AND JANG, H. Effect of grain size on the electrical failure of copper contacts in fretting motion. *Tribology International* 111 (2017), 39 – 45.
- [43] OLMSTED, D. L., FOILES, S. M., AND HOLM, E. A. Survey of computed grain boundary properties in face-centered cubic metals: I. grain boundary energy. *Acta Materialia* 57, 13 (2009), 3694 – 3703.
- [44] OSHER, S., AND SETHIAN, J. A. Fronts propagating with curvature-dependent speed: Algorithms based on Hamilton-Jacobi formulations. *Journal of Computational Physics* 79, 1 (1988), 12–49.
- [45] PETERSON, N. L. Grain-boundary diffusion in metals. *International Metals Reviews* 28, 1 (1983), 65–91.
- [46] PRIESTER, L. *Grain Boundaries: From Theory to Engineering*. 2013.
- [47] PROKOSHKINA, D., ESIN, V. A., WILDE, G., AND DIVINSKI, S. V. Grain boundary width, energy and self-diffusion in nickel: Effect of material purity. *Acta Materialia* 61, 14 (2013), 5188 – 5197.
- [48] RANDLE, V., HU, Y., AND COLEMAN, M. Grain boundary reorientation in copper. *Journal of Materials Science* 43, 11 (2008), 3782 – 3791.
- [49] READ, W. T. *Dislocations in crystals*. McGraw-Hill Book Company, INC., 1953.
- [50] READ, W. T., AND SHOCKLEY, W. Dislocation models of crystal grain boundaries. *Physical Review* 78, 3 (1950), 275–289.
- [51] RENAT T., S. Anomalous grain boundary diffusion: Fractional calculus approach. *Advances in Mathematical Physics* 2019 (2019).
- [52] RONEVICH, J. A., D’ELIA, C. R., AND HILL, M. R. Fatigue crack growth rates of X100 steel welds in high pressure hydrogen gas considering residual stress effects. *Engineering Fracture Mechanics* 194 (2018), 42 – 51.
- [53] SCHEIBER, D., PIPPAN, R., PUSCHNIG, P., AND ROMANER, L. Ab initio calculations of grain boundaries in bcc metals. *Modelling and Simulation in Materials Science and Engineering* 24 (2016).
- [54] SUTTON, A. P., AND BALLUFFI, R. W. *Interface in Crystalline Materials*. Oxford University Press, 1995.

- [55] SUZUOKA, T. Lattice and grain boundary diffusion in polycrystals. *Transactions of the Japan Institute of Metals* 2, 1 (1961), 25–32.
- [56] TORIBIO, J., VERGARA, D., AND LORENZO, M. Role of in-service stress and strain fields on the hydrogen embrittlement of the pressure vessel constituent materials in a pressurized water reactor. *Engineering Failure Analysis* 82 (2017), 458 – 465.
- [57] UESUGI, T., AND HIGASHI, K. First-principles calculation of grain boundary energy and grain boundary excess free volume in aluminum: role of grain boundary elastic energy. *Journal of Materials Science* 46, 12 (2011), 4199 – 4205.
- [58] WHIPPLE, R. T. P. Concentration contours in grain boundary diffusion. *The London, Edinburgh, and Dublin Philosophical Magazine and Journal of Science* 45, 371 (1954), 1225–1236.
- [59] WOLF, D. On the relationship between symmetrical tilt, twist, "special", and "favored" grain boundaries. *J. Phys. Colloques* 46, 4 (1985), 197–211.
- [60] WOLF, D. Correlation between energy and volume expansion for grain boundaries in FCC metals. *Scripta Metallurgica* 23, 11 (1989), 1913 – 1918.
- [61] WOLF, D. Structure-energy correlation for grain boundaries in F.C.C. metals - III. symmetrical tilt boundaries. *Acta Metallurgica et Materialia* 38, 5 (1990), 781 – 790.
- [62] ZHAO, J., WANG, G. X., YE, C., AND DONG, Y. A numerical model coupling diffusion and grain growth in nanocrystalline materials. *Computational Materials Science* 136 (2017), 243 – 252.